Towards Force-Correlated Ultrasound Volume Elastography

by

Moritz Alexander Graule

BSc and MSc in Mechanical Engineering
ETH Zurich, Switzerland, 2013 and 2015

Submitted to the Department of Mechanical Engineering
in partial fulfillment of the requirements for the degree of
Master of Science in Mechanical Engineering

at the

Massachusetts Institute of Technology

September 2017

Author. Signature redacted ....
Department of Mechanical Engineering
August 25, 2017

Certified by...... Signature redacted ....
Brian W. Anthony
Principal Research Scientist, Department of Mechanical Engineering
Thesis Supervisor

Accepted by............ Signature redacted ....
Rohan Abeyaratne
Professor of Mechanical Engineering
Chairman, Department Committee on Graduate Theses

Towards Force-Correlated Ultrasound Volume Elastography

by
Moritz Alexander Graule

Submitted to the Department of Mechanical Engineering
on August 25, 2017 in Partial Fulfillment of the
Requirements for the Degree of Master of Science in
Mechanical Engineering

ABSTRACT

This thesis proposes three ultrasound-based methods that enable quantification of tissue and organ properties with potential applications as non-invasive, image-based biomarkers: force-controlled elasticity quantification for the identification of strain hardening; registration and segmentation of B-mode images to measure organ volumes; and force-correlated three-dimensional elasticity maps.

In order to allow for the simultaneous collection of tissue elasticity and compressive force, a shear wave elasticity enabled ultrasound probe was integrated with a load cell which measured the sonographer-applied preload. The device was used to demonstrate the strong preload dependence of elasticity in ex-vivo bovine liver, illustrating the importance of accounting for preload when using elastography to assess tissue health. Finally, this device enables the quantification of strain hardening as an additional metric for tissue health.

The capability organ volume measurements through freehand ultrasound imaging was demonstrated in a clinical study in which kidney volumes were obtained from ultrasound sweeps and compared to ground truth data from CT scans. While the technology needs to be refined to achieve better agreement between the measured volumes, the initial results of this ongoing study allowed for the identification of an ideal acquisition strategy. These findings will inform future data collection to achieve an improved accuracy.

The acquisition of three-dimensional force-correlated elasticity maps was demonstrated on a phantom with the successful detection of a high-stiffness lesion embedded in bulk material. The presented technology has the potential to be a quantitative replacement for manual palpation. Given further refinement, this technology could be used to replace needle biopsy in various diseases in which progression correlates with tissue stiffness, such as thyroid nodules or liver fibrosis and cirrhosis. Our method, unlike the inherently localized needle biopsy, allows for the assessment of tissue over a broad volume, potentially improving reliability and repeatability in diagnosing and staging diffuse diseases.

Thesis Supervisor: Brian W. Anthony
Title: Principal Research Scientist, Department of Mechanical Engineering

ACKNOWLEDGEMENTS

I have dreamed of coming to MIT since childhood. As such, I would like to express my gratitude to everyone who made this possible.

First and foremost, I am grateful to my supervisor Dr. Brian Anthony for giving me the opportunity and resources to pursue research in his lab; and Leslie Regan and her office whose boundless effort to support graduate students helps making MIT MechE a great place to learn. I would also like to extend my thanks to our amazing collaborators, in particular: Dr. Anthony Samir, Dr. Qian Li, and Dr. Manish Dhyani at MGH for providing insights into the needs of patients and doctors and working with us to translate our technology to the clinic; and Dr. Hua Xie and Dr. Man Nguyen at Philips Research for enabling us to closely integrate our work with state of the art ultrasound imagers and always being available to answer practical and theoretical questions.

To my friends at and around MIT: thanks fam, you made my time in Cambridge fun! To my friends back home in rural Switzerland: our BBQ's were always worth the trip from Boston to Zurich!

Lastly, I am deeply grateful to my parents and siblings for supporting, motivating and encouraging me. Coming home to hang out with you has always been both relaxing and energizing, and I already look forward to our next annual wakeboard session.

CONTENTS

FIGURES

TABLES

CHAPTER

1

INTRODUCTION

Manual palpation of tissue as a means to distinguish between healthy and unhealthy tissue has been applied for centuries [1], if not millennia, with the quote ’*the living are soft and yielding; the dead are rigid and stiff*’ attributed to mythical Chinese philosopher Laozi, who is said to have lived more than two thousand years ago. Since then, numerous scientific studies have shown an increased stiffness in unhealthy tissue [2]–[7].

The qualitative method of manual palpation is still used widely today, for example in the (self-) discovery and early assessment of thyroid nodules [6], [8]; breast and testicular cancer [9]; and musculoskeletal conditions [10]–[13]. Suspicious initial findings are commonly followed up with further examinations, such as needle biopsies to determine the malignancy of thyroid nodules [6], [14]; or mammography to screen for or confirm the presence of breast nodules [15]. As manual palpation is not quantitative and can show large intra- and inter-operator variation, it can lead to the oversight of small nodules [16]; cause unnecessary removal of benign breast lesions [17]; and is often not suited for the reliable tracking of disease progression.

Furthermore, stiffness has been shown to correlate with disease progression in tissue that is not accessible to manual palpation. In particular, severe cases of non-alcoholic fatty liver disease (NAFLD) result in an increased liver stiffness [4], [7]. NAFLD is characterized by an increased amount of fatty tissue in the liver in patients with no know history of excessive alcohol consumption [18]. Affecting a large percentage of the world population and being a major cause of liver transplantations [19], NAFLD generates significant personal suffering and health care costs. NAFLD can be separated into simple fatty liver (hepatic steatosis), non-alcoholic steatohepatitis (NASH; characterized by an increased fat content and inflammation) [20], [21], and may progress to fibrosis (scarring of liver tissue), cirrhosis (strong scarring), liver failure and liver carcinoma [22]–[26].

The stages of NAFLD and its potential progressions are currently assessed using needle biopsies [20]. Due to the diffuse nature of these diseases, and the inherently local nature of needle biopsy, misclassifications are possible [27], [28].

The above examples illustrate the need for a reliable method to quantify tissue elasticity not only locally, but as a three-dimensional stiffness map to support the non-invasive diagnosis and staging of various diseases. The following sections highlight recent advances towards that goal.

1.1 Recent Advances in Ultrasound Imaging

1.1.1 Ultrasound Elastography

Ultrasound elastography refers to different methods that enable the quantification of tissue stiffness using ultrasound, which have the potential to provide a more quantitative approach to disease diagnosis and staging.

Ultrasound elastography can broadly be grouped into strain elastography and shear wave elastography. Strain elastography relies on Hooke's law, which relates the Young's modulus E to stress σ and strain ε as $E = \sigma/\varepsilon$ in linearly elastic materials [29]. The relative displacements of tissue regions are tracked to compute a region-dependent map containing strain and relative elasticity. Traditionally, neither the transducer preload nor other metrics indicating stress are measured in strain elastography, which makes it impossible to compute the absolute tissue elasticity. Instead, the resulting maps only show relative tissue stiffnesses [29]–[31].

Shear wave elastography methods generally rely on tracking the propagation of shear wave wavefronts, the speed of which depends on the elasticity of the investigated medium. High frequency ultrasound imaging is used to track the displacements of features at a high resolution to track these wavefronts. The waves can either be generated by external thumping on the surface of the tissue under investigation, or by using the ultrasound transducer to send a high energy acoustic pulse into the tissue [29]–[31].

1.1.2 3D Ultrasound Imaging

Traditionally, ultrasonic imaging is a two-dimensional modality. Expanding it to enable volume imaging through the spatial registration of images promises a number of advantages. For example, it can lead to a higher reliability in the clinically relevant measurements of tissue properties and geometries, since these measurements become less dependent on probe placement as with 2D probes [32], [33]. It can further enable a more accurate registration with other volume imaging modalities and has been shown to be useful in guiding biopsy needles [34] and surgical tools [35]. Additionally, 3D ultrasound imaging, given sufficient resolution and geometric accuracy, could provide a cost-effective alternative to MRI and CT scans.

The registration of ultrasound image slices can be achieved by mechanically translating, sweeping or rotating a one-dimensional array in a controlled fashion [36], [37]; using a 2D transducer array with known relative transducer element positioning [38]; or tracking of a probe's motion during freehand scans through external cameras [39], [40], electromagnetic tracking devices [40], or cameras mounted on the probe [41], [42].

1.1.3 Ultrasound Segmentation and Classification

An extensive review of segmentation algorithms for ultrasound images is given in [43]. Most approaches are implementations of algorithms that have previously been established in the broader field of computer vision, with adjustments to tackle the specific challenges arising when working with ultrasound images. Select key contributions in ultrasound segmentation include the use of information in the frequency domain [44] (as opposed to purely intensity-based approaches), the application of artificial neural networks [45] and the use of a template and its physically meaningful deformations[46]. More recent approaches include a wavelet-based method to differentiate between healthy and diseased liver tissue [47]; as well as a method to detect and classify breast tumors relying on a modified Normalized Cut approach [48].

CHAPTER

2

FORCE-CORRELATED ULTRASOUND ELASTOGRAPHY

The following chapter describes the development and evaluation of an ultrasound probe modified to simultaneously record preload and tissue stiffness at various depths by tracking the propagation speed of acoustically excited shear waves. This is an extension of previous work on the design of ultrasound probes for force-correlated B-mode imaging [49]–[51].

2.1 Materials and Methods

2.1.1 Experimental Setup

2.1.1.1 Ultrasound imaging system

A Philips EPIQ ultrasound imager with a curved C5-1 probe was used to acquire the images (both from Philips North America, Andover, MA; provided by Philips Research, Cambridge, MA). ElastPQ, the system's integrated shear wave imaging solution, was used to quantify the average sample elasticity within a small, manually selected target area.

2.1.1.2 Force-measurement system with manually adjustable probe mount

A custom hand-held force measurement device was integrated with the Philips C5-1 probe to record the preload on the probe during image acquisition. The assembly consists of a custom-fit, ergonomic outer shell housing the US probe, an accelerometer (Adafruit ADXL335, Adafruit Industries, New York City, NY) and a load cell (*FUTEK* LSB200, *FUTEK* Advanced Sensor Technology, Inc, Irvine, CA) to measure the force between the probe and the outer shell (and thus the sonographer or probe mount). The shape of the probe was scanned using a NextEngine Desktop

3D Laser Scanner (Model 2020i, NextEngine, Inc., Santa Monica, CA). The clamp to connect the probe to a load cell and the outer shell as mechanical ground were designed in SolidWorks (Version 2015, Solid Works Corporation, Concord, MA) and printed from ABS plastic using a Stratasys uPrint (Stratasys, Ltd., Eden Prairie, MN). The shell customization process is illustrated in Figure 2.1. Figure 2.2 shows the finalized force measurement assembly.

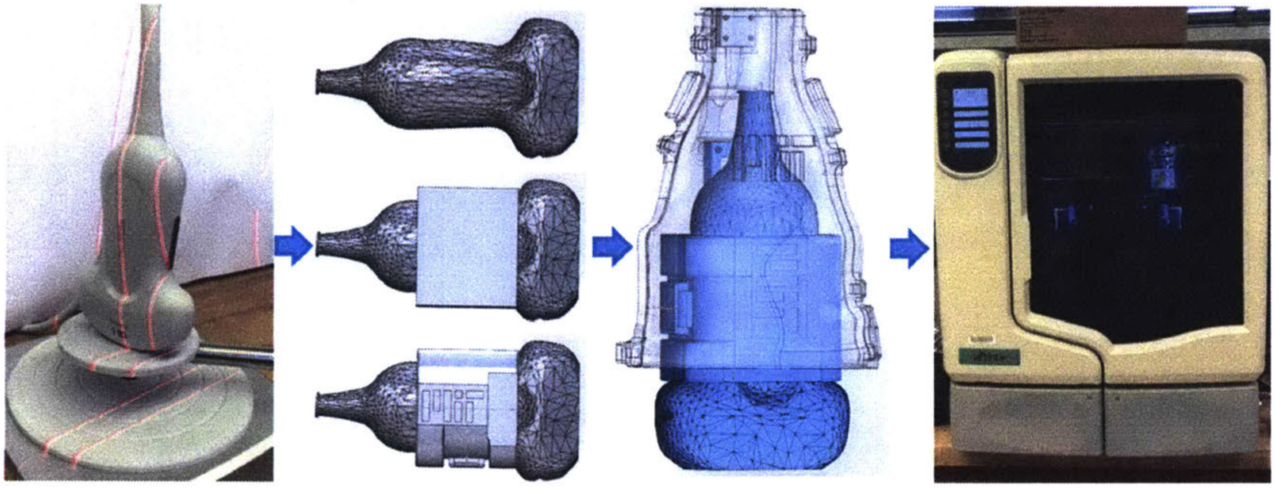

Figure 2.1: Customization-process for force-measurement assembly

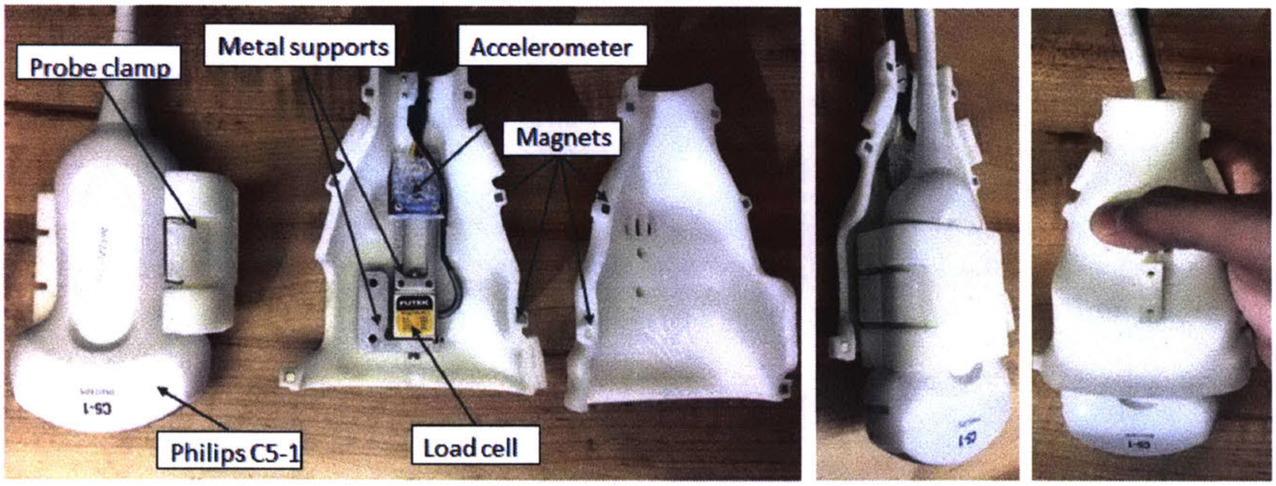

Figure 2.2: Hardware to record force-correlated ultrasound images and elastographs

The preload data was hardware conditioned (*FUTEK* CSG110) and the preload and accelerator data was collected through a data acquisition card (USB-6001 DAQ, National Instruments, Austin, TX) with a laptop running custom LabVIEW (Version 2015, National Instruments) code.

The force measurement device was then mounted onto a manually operated lead screw as shown in Figure 2.3 to allow for measurements at varying preload.

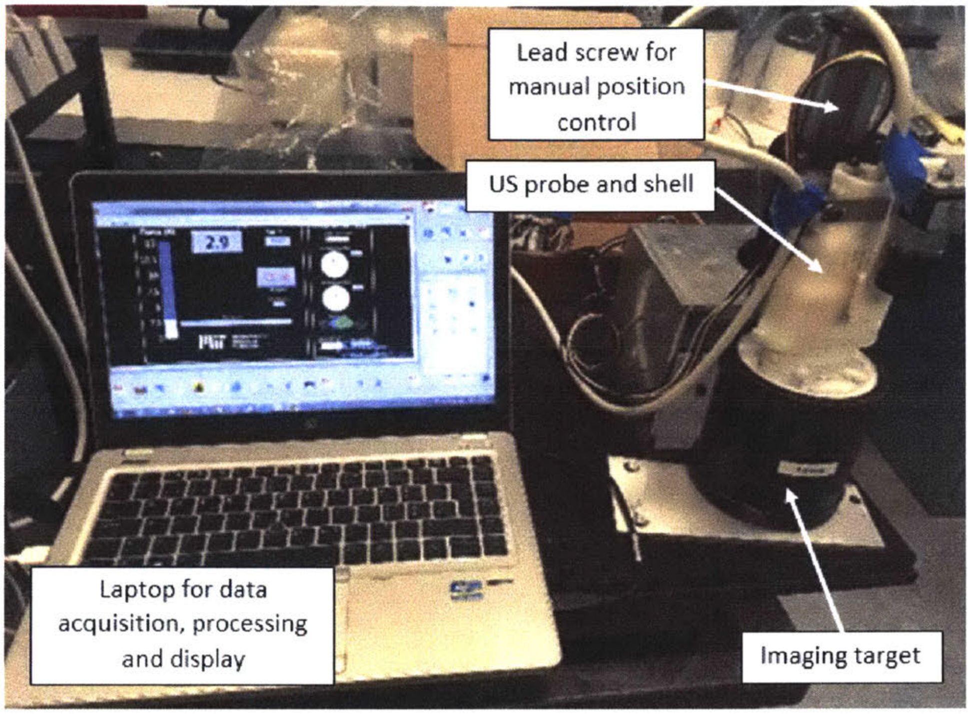

Figure 2.3: Experimental setup for force-correlated elastography

2.1.2 Imaging Targets

2.1.2.1 Liver phantoms

A liver mimicking phantom with a nominal stiffness of 3 kPa, corresponding to healthy liver tissue [7], [52], [53], were obtained from CIRS (Shear Wave Liver Fibrosis Phantom Model 039, Computerized Imaging Reference Systems, Inc., Norfolk, VA).

2.1.2.2 Ex-Vivo bovine liver

Ex-vivo bovine liver samples were obtained from a local butcher. The livers were degassed in immersion for four hours using a Welch vacuum pump (Model 2561B – 50, Gardner Denver, Milwaukee, WI) to reduce the amount of air bubbles for improved ultrasound imaging quality. Three different livers were characterized.

2.1.3 Protocol

For each acquisition series, the probe was first positioned such that its face is in light contact with a gel pool on top of the sample. This position was defined as the 'unloaded' case and the bias force in the acquisition software was set such that the recorded preload reads as 0 N.

Local elasticity measurements were taken for preloads ranging from 0 – 3 N in ex-vivo bovine livers and from 0 – 7 N in the liver phantom (force increased in 1 N intervals by manually adjusting the probe position using a lead screw). At least three elasticity measurements were taken for each sample at each preload using the system's ElastPQ method.

Increasing the preload may lead to relative displacement between the imaged region in the sample and the probe due to tissue compression. To account for this, the region of interest for the ElastPQ measurements was moved to be coincident with the previous region as closely as possible whenever the preload was varied.

2.2 Results

The results of the force-correlated ultrasound elastography measurements are shown in Figure 2.4. The reported values are the average of at least three measurements. Error bars represent one standard deviation.

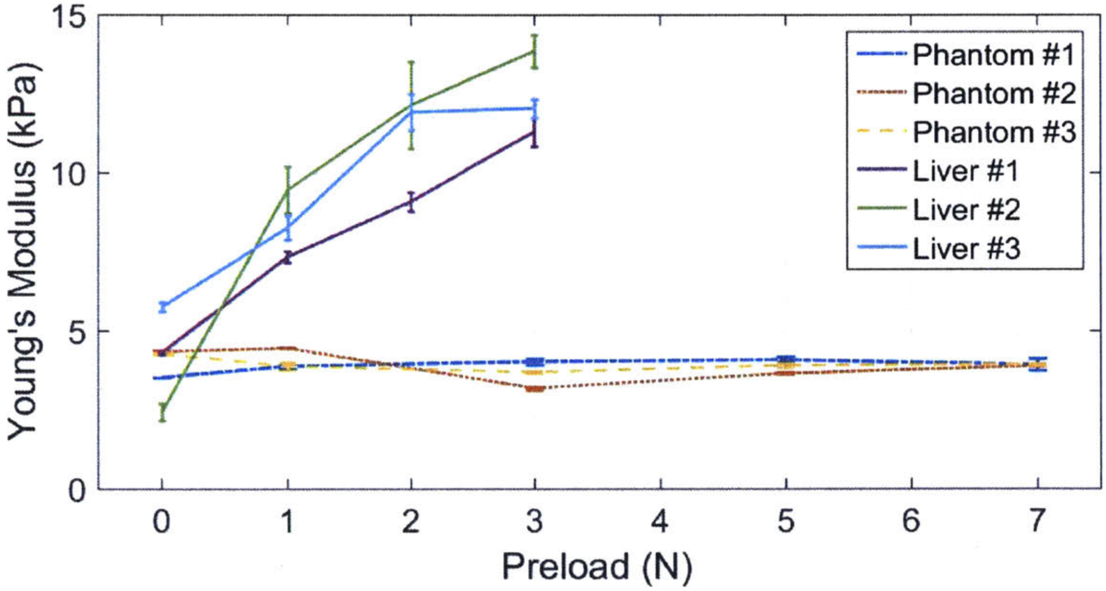

Figure 2.4: The dependence of preload on Young's Modulus in phantoms and ex-vivo tissue.

2.3 Discussion

The stiffness of the phantoms did not change with preload over the observed force range. The ex-vivo bovine livers, however, showed significant strain-hardening with a two- to fivefold increase in Young's Modulus when the preload was increased from 0 N to 3 N. A similar nonlinear stress-strain response was found in human biceps and quadriceps [54].

The standard deviations for a given force within a measurement series are generally higher in ex-vivo tissue than in the phantoms. This is likely caused by the fact that the ex-vivo tissue is much more heterogeneous. Thus, small changes in the region of interest for the ElastPQ measurements (caused by either displacement or changes in compression) have a higher impact in ex-vivo tissue. Heterogeneities between the probe and the target region further affect the high-energy acoustic pulse used to trigger the shear wave for ElastPQ and cause imprecisions in tracking said shear wave.

Recent research suggests that the variation in image-based biomarkers, such as gray scale intensity, decreases with increasing preload [55]. For tissues displaying strain hardening, a similar effect would be expected in ultrasound elastography, as an absolute variation in operator-applied force will have a reduced effect on reported stiffness at higher preload. It may therefore be beneficial to apply higher preloads when measuring tissue stiffness using shear wave elastography.

2.4 Summary

Force measurement capability was integrated with a commercial ultrasound probe capable of shear wave elastography to enable the simultaneous measurement of tissue elasticity and preload applied to the tissue under investigation. This device was used to determine the stiffness of a liver mimicking phantom and ex-vivo bovine livers at varying compressive forces. While the biological tissue showed significant strain hardening, the elasticity of the phantom was independent of compression.

These results demonstrate the non-linear stress-strain relationship in biological tissue, highlighting the importance to account for the sonographer-applied preload when using tissue stiffness as a biomarker in diagnosing and staging diseases. Strain-hardening-induced variability in measured elasticity is likely more pronounced in near-surface tissue. For deeper tissue, such as in-vivo liver, the surrounding tissue and bones likely absorb a significant part of the preload, reducing the compression, and thus the strain-hardening, of the tissue under investigation.

While the constant elasticity of the phantoms may be a desired property in many cases of experimental technology validation, it is worth noting that they do not accurately represent the mechanical behavior of biological tissue.

Furthermore, the nature of the non-linearity in the stress-strain relationship may provide an additional biomarker to distinguish between healthy and unhealthy tissue.

CHAPTER

3

TOWARDS ULTRASOUND VOLUMETRY

In cooperation with Dr. Anthony Samir's team at the Massachusetts General Hospital (Boston, MA; MGH), we conducted a clinical study to show the feasibility of freehand 3D ultrasound imaging based on an approach previously demonstrated in a controlled laboratory environment [41]. Specifically, the study aimed to demonstrate the capability to measure kidney volumes using freehand ultrasound probes with a one-dimensional transducer array.

In brief, the approach relies on an ultrasound probe equipped with a conventional camera directed such that it takes videos of the skin during the ultrasound acquisition (see Figure 3.1). Specific features, ideally with sufficiently unique descriptors, can then be extracted from the skin video frames and matched to the corresponding features in subsequent frames. The camera pose can then be estimated from these correspondences, and the ultrasound probe pose can be obtained by applying the known rigid transformation between camera and probe coordinate systems. Knowledge of the probe poses finally allows for the registration of ultrasound based volumes. A detailed discussion of the underlying theory can be found in [41], [56].

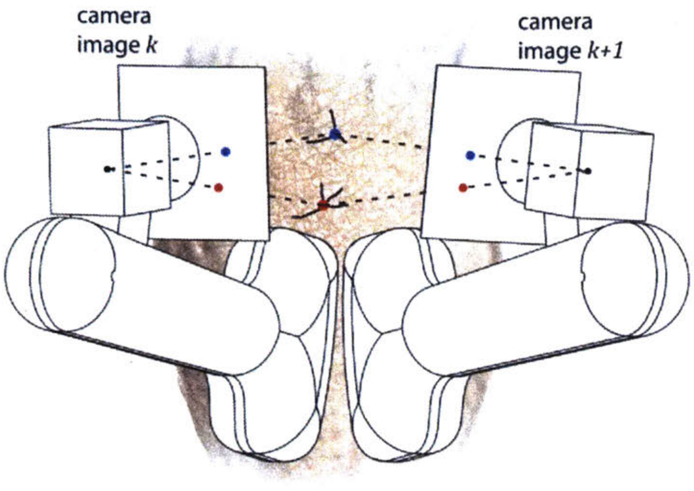

Figure 3.1: Depiction of ultrasound probe equipped with camera to infer pose from skin images

3.1 Clinical Motivation

The quantification of volumes of geometrically defined tissue regions (such as organs, muscles or lesions) has various clinical applications. Possible use cases range from the assessment of tumor progression [6], muscle dystrophy [57] or sarcopenia [58]; to assessing the function of the kidneys [59], the heart [60], and other organs [61], [62].

Renal volume has been identified as a biomarker for autosomal dominant polycystic kidney disease (ADPKD) [63]–[65] and is related to kidney function [59], which in turn is an important indicator of chronic kidney disease [66]. An increased renal volume in diabetics is further associated with a heightened risk for nephropathy [67].

3.2 Algorithms for Ultrasound Volumetry

3.2.1 Tracking Tissue Interfaces in Ultrasound Images

A method to detect tissue interfaces and track them throughout ultrasound force and volume sweeps was developed as a step towards an automated segmentation of kidney volumes. The method is applicable to a broad set of problems that requires the propagation of features throughout ultrasound sweeps of either varying location or compression, such as segmentation; registration of ultrasound images from longitudinal studies; registration between volumes of different modalities; strain-elastography; or volumetry of various organs and muscles. Figure 3.2

shows a demonstration of the methods capability on a constant-position acquisition with continuously increasing preload. The underlying algorithm is described below.

Preprocessing / edge detection for each frame I_{in} within in the sweep:

1. Normalize intensity range to [0,1]
2. Correct for brightness drift
   - Filter I_{in} with small Gaussian blur (3x3 or 5x5) to remove noise: I_{C1}
   - Filter I_{C1} with large Gaussian blur to get illumination drift: I_{C2}
   - $I_C = I_{C1} - I_{C2}$
3. Compute intensity-based likelihood of a pixel being an edge: I_{L1}
   - $I_C = \max(I_C, 0)$ (explanation: wherever $I_C < 0$, there is certainly no edge)
   - Set pixels with value < mean(I_C) in I_C to 0 (explanation: this assumes that less than half the pixels are actually edges and the intensity distribution around edges is sufficiently small)
4. Introduce connectivity requirement for true edges to obtain I_{L2}
   - Convolute I_{L1} with a 3x3 matrix of ones to obtain I_{L2}
   - $I_{L2} = I_{L1}/3$
   - Threshold I_{L2}: set all values > 1 to 1 (explanation: assuming a binary edge map, every pixel neighboring at least 2 edge pixels has now the value 1). Adjust threshold from 1 to 0.9 for non-binary case.
   - Threshold set all values < 0.25 to 0 (explanation: this assumes that less than half the pixels are actually edges and the intensity distribution around edges is sufficiently small)
5. Convolute with Gabor wavelets distributed evenly across the relevant feature directions and sizes and threshold to obtain binary edge map

Edge tracking between frames I_{i-1}, I_i, I_{i+1}

1. In edge map $I_{L2,i}$, label connected edges and sort edges by size
2. For each edge larger than a selected minimum size (10 was shown to work well), search corresponding edge in frames $I_{L2,i-1}, I_{L2,i+1}$
   - Obtain bounding box around edge

  - Project bounding box into search frames ($I_{L2,i-1}$ and $I_{L2,i+1}$). Use template matching with a maximum search distance of 20 pixels to find corresponding edge.

3. Smooth edge trajectories across multiple frames

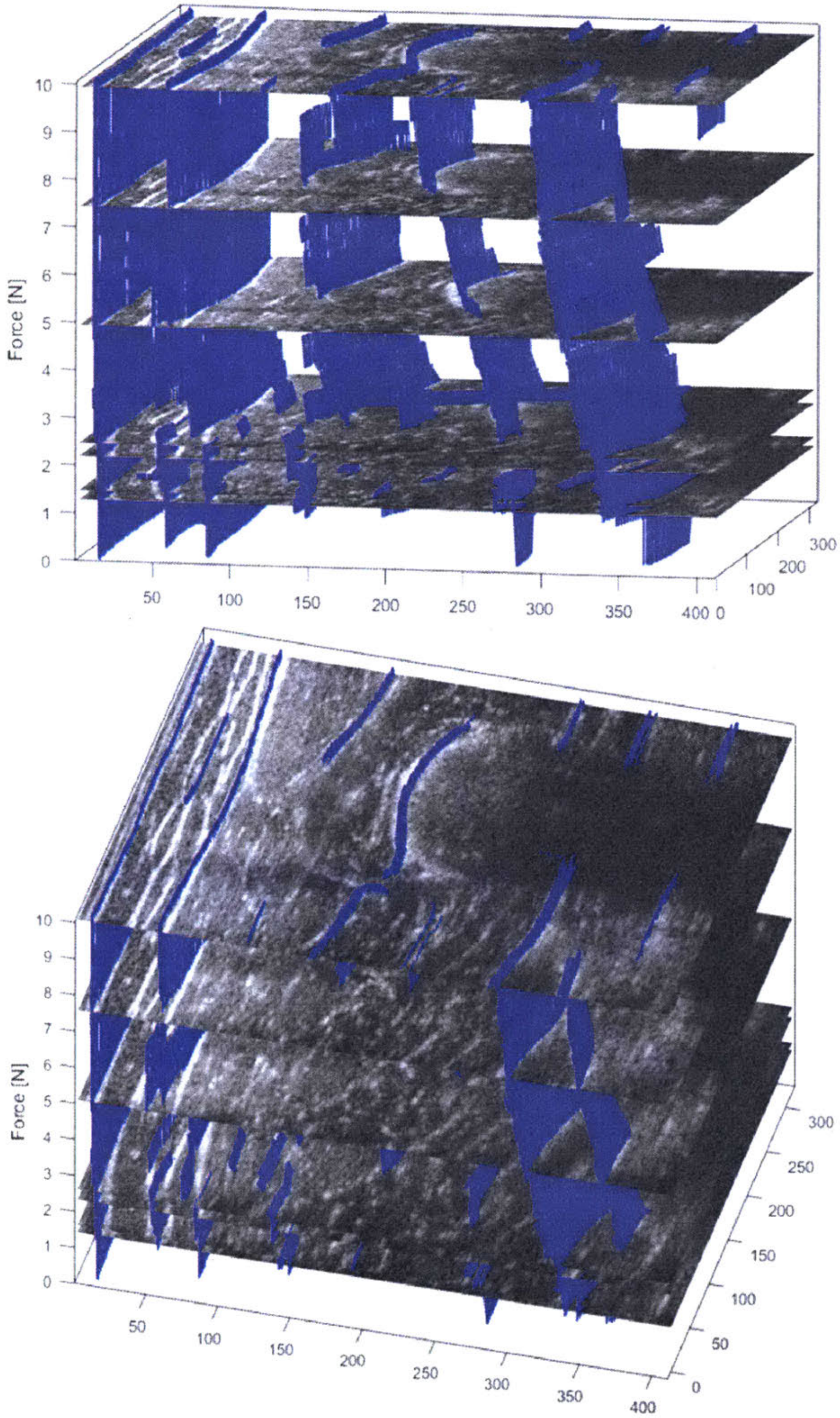

Figure 3.2: Automated propagation of tissue interfaces in ultrasound images

3.3 Materials and Methods

3.3.1 Clinical Study Overview

Subjects for this IRB approved study (Protocol Number 2015P001882/MGH at MGH) were recruited from a pool of patients who had undergone a computed tomography (CT) scan at MGH within up to three months prior to the targeted study date. The images from the CT scan were used as ground truth data on kidney structure and volume. Table 3.1 gives an overview of the clinical data collected on each of the patients. Each examination lasted approximately one hour.

Table 3.1: Overview of data collected in clinical study

Patient number	Acquisition modalities	Kidney scanned	Number of scans	Notes
1	- Ultrasound - Camera - Load cell to measure preload	right	14	GE EM tracking deactivated (patient health incompatible with EM waves)
2	- Ultrasound - Camera - GE EM tracking - Load cell to measure preload	left / right	25	
3	- Ultrasound - Camera - GE EM tracking - Load cell to measure preload	left / right	27	
4	- Ultrasound - Camera - Load cell to measure preload	left / right	22	Technical issues with GE EM tracking
5	- Ultrasound	left / right	24	

	- Camera - GE EM tracking - Load cell to measure preload			
6	- Ultrasound - Camera - GE EM tracking - Load cell to measure preload	left / right	26	

For each patient, the subject's kidneys (left and right) were scanned by professional sonographers using the hardware described in Section 0. Table 3.2 lists the different types of acquisition sweeps that were used (visualized in Figure 3.3). Each sweep was acquired at least twice, once with low and once with high preload. The sonographers were instructed to aim for a force below 10 N for the low preload acquisition, and above 10N for the high preload acquisition. Before each sweep, the sonographers identified the optimal acoustic window for the sonogram, optimizing probe-to-patient position and breathing to minimize shadows caused by bowel gas and ribs. The sonographers were instructed to limit the motion to either purely translational, or purely rotational, as much as other circumstances allow (for example, a patient's physique or the nature of the acoustic window). This simplifies volume reconstruction, as it is challenging to distinguish between small rotations and small translations by tracking optical features. The videos form the ultrasound imager and the optical camera were examined after each sweep and the acquisition was repeated if either of them were deemed to be of insufficient quality.

Table 3.2: Probe sweeping motions used in clinical study

Probe position on body	Sweep direction relative to kidney	Sonographer-applied preload (qualitative)	Targeted motion
Lateral	Transverse	Low	Pure translation
Lateral	Transverse	High	Pure translation
Lateral	Longitudinal	Low	Pure translation
Lateral	Longitudinal	High	Pure translation
Lateral	Fan	Low	Pure rotation

Lateral	Fan	High	Pure rotation
Back	Transverse	Low	Pure translation
Back	Transverse	High	Pure translation
Back	Longitudinal	Low	Pure translation
Back	Longitudinal	High	Pure translation

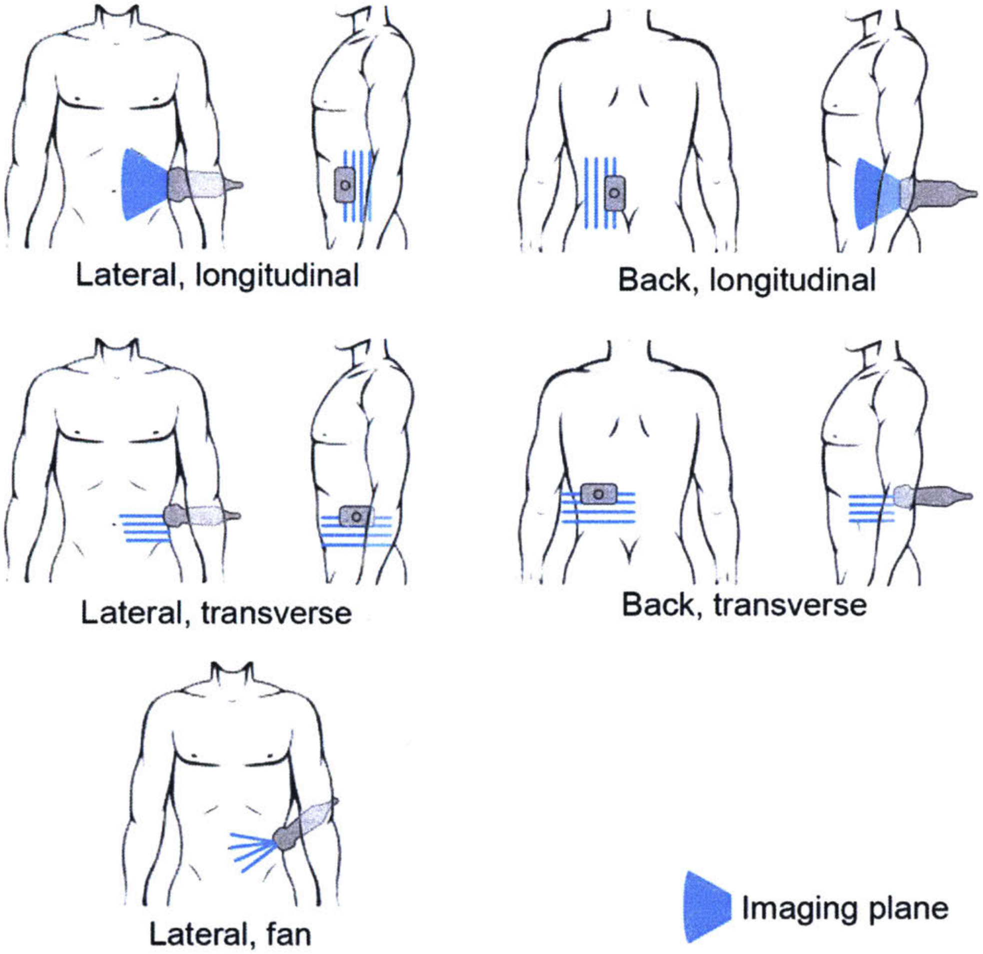

Figure 3.3: Probe sweeping motions used in clinical study

3.3.2 Hardware

3.3.2.1 Ultrasound imaging system

A GE Logiq E9 ultrasound imager with a curved C1-5 probe was used to acquire the B-mode images (both from General Electric Company, Boston, MA).

3.3.2.2 Electromagnetic position tracking: system description and characterization

An off-the-shelf electromagnetic position tracking system from GE was used to acquire information on the position and orientation (further referred to as pose) of the US probes. The system consists of a stationary antenna emitting electromagnetic waves, which is placed in close proximity to the patient, and two electromagnetic receivers fixed to the US probe through a mounting bracket. The system integrates with the ultrasound imaging system, which computes a pose estimate based on the signals received by the two sensors.

As the information provided by the manufacturer was incomplete, trial runs were conducted to identify the structure of the raw data provided by the electromagnetic position tracking system. In these trials, the probe was moved along predetermined trajectories using a rigid plate with a grid to guide the motion. The trajectories consisted of isolated translations and rotations along each axis. A total of 23 trial sequences were recorded with the different motion patterns as described in Appendix A.1. An exemplary trajectory from this characterization is shown in Figure 3.4. The characterization allowed for the identification of the recorded position data, but also showed that the position data tends to contain multiple arbitrary sign changes, strongly reducing the usability of the EM tracking data for volume reconstruction.

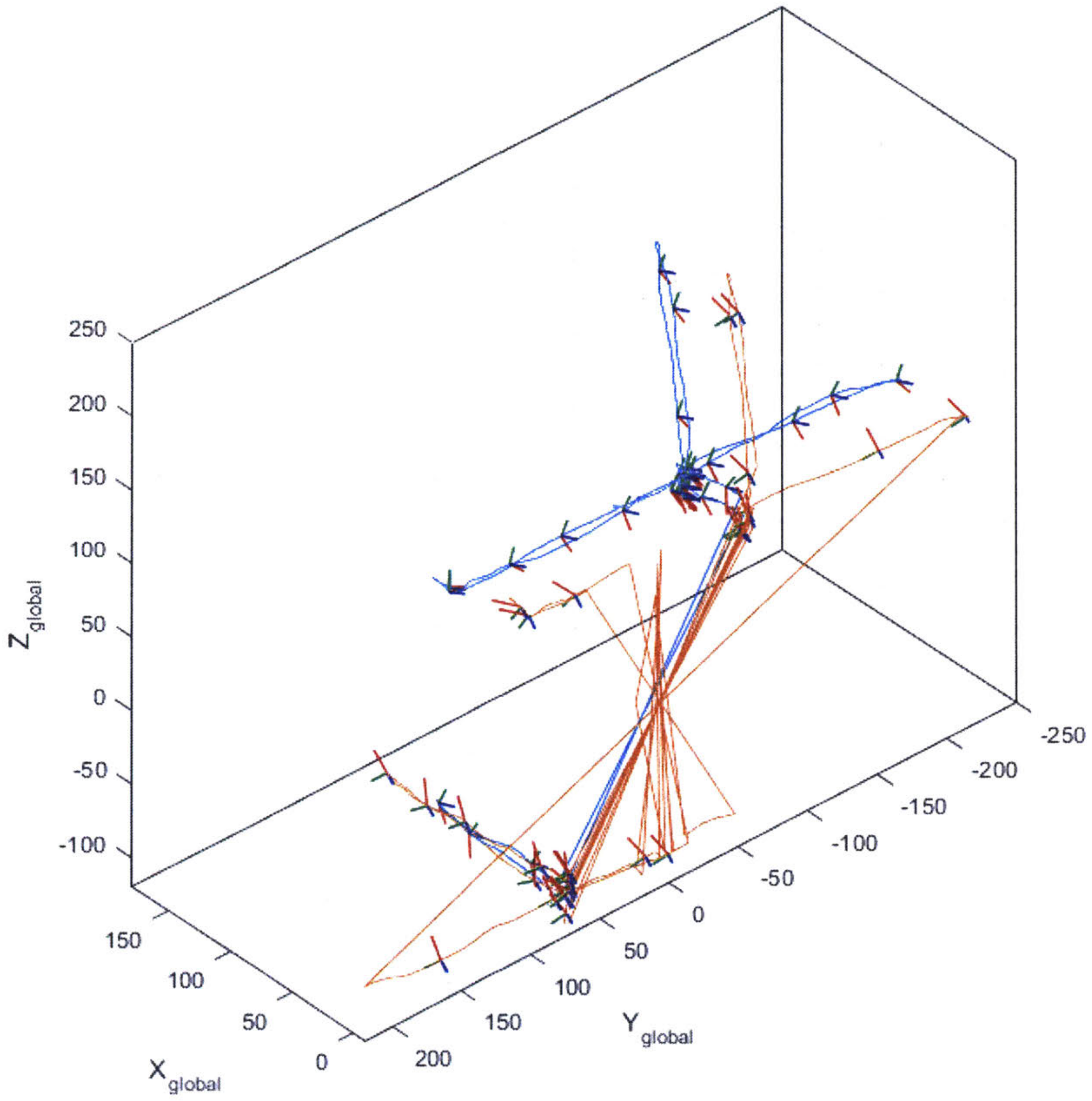

Figure 3.4: Exemplary EM tracking data for continuous translation

3.3.2.3 Force-measurement system with externally mounted camera

A custom hand-held force measurement device was built around the GE C1-6 probe with the same customization procedure and identical components as described in Section 2.1.1.2. In addition, a commercially available camera (acA2040-90uc, Basler AG, Germany) was mounted to the outside of the shell. The shell design was further adjusted to allow for the mounting of a commercial probe position tracking system from GE (see Section 3.3.2.2) based on two electromagnetic sensors. A photograph of the assembly excluding the GE position tracking hardware, and one including it, are shown in Figure 3.5, and Figure 3.6 respectively. In addition, an external light source was used to ensure good lighting conditions on the subject's skin area that was filmed with the optical camera.

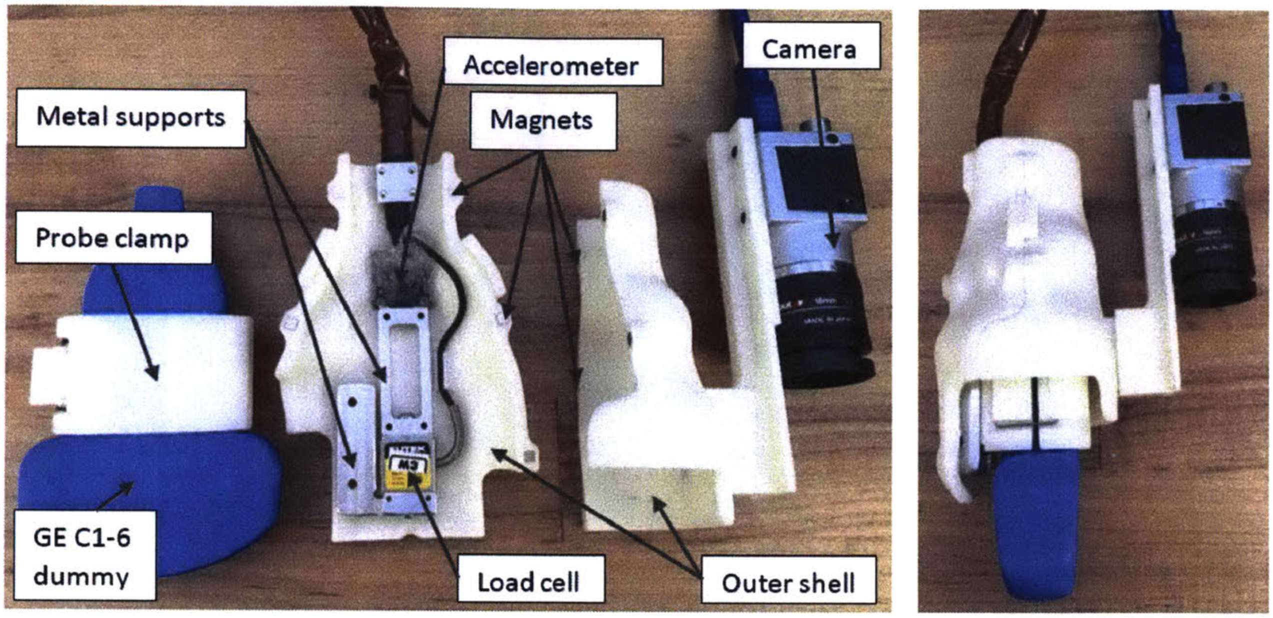

Figure 3.5: Hardware to record force-correlated ultrasound images and skin images

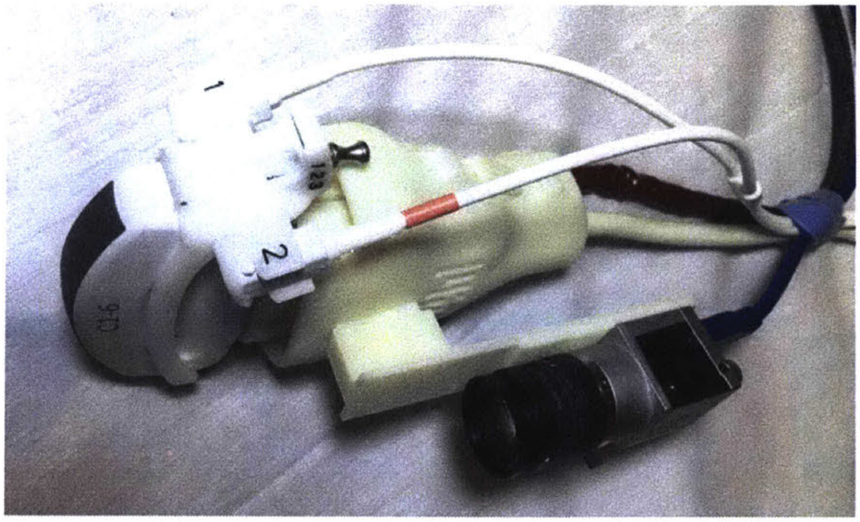

Figure 3.6: Hardware to record force-correlated ultrasound images and skin images including electromagnetic sensors and mounting bracket.

3.3.3 Software

The LabVIEW program described in Section 2.1.1.2 was modified to allow for the parallel, yet synchronized, acquisition of images of the patients skin via the camera and the preload on the US probe via the load cell. A producer-consumer structure as shown in Figure 3.7 was implemented to collect and save color images at up to 30 frames per second on a standard desktop computer using a solid state hard drive. The producer-consumer buffer structure allows to parallelize image acquisition and writing, leading to a higher and more consistent frame rate. The program stores the frames in binary format for higher writing speeds. A second program was written to convert those binary files to a video in *.avi format post acquisition. Image acquisition is highest for empty hard drives with free space much larger than required to save one video and can be improved by assigning a high priority to the LabVIEW instance running the acquisition code.

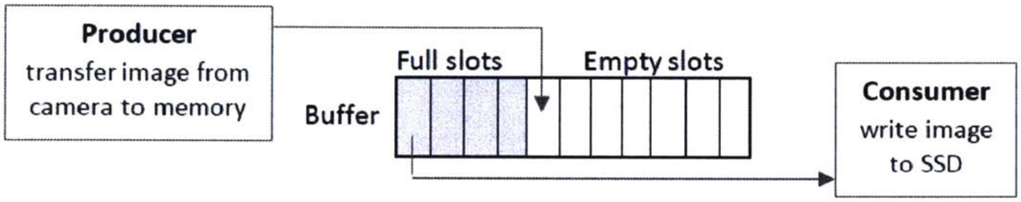

Figure 3.7: Producer-consumer structure to parallelize image acquisition and writing

3.4 Results and Discussion

3.4.1 Kidney Volumes from CT Scans

The kidneys were manually annotated and segmented by a technically-trained lay person in the CT volumes using 3D Slicer [68]. The resulting kidney volumes are shown in Table 3.3.

Table 3.3: Kidney volumes from CT scans

Patient number	Left kidney volume [ml]	Right kidney volume [ml]	Sex
1	256.07	298.59	M
2	209.37	199.28	M
3	151.26	190.63	F
4	151.52	139.39	F
5	231.89	196.847	M
6	166.18	183.673	F

3.4.2 Comparison of Acquisition Strategies

An ideal acquisition sweep for volume reconstruction is characterized by either a pure rotational or translational motion, whereas a pure translational motion (ideally perpendicular to the ultrasound image frame) is preferred. In order to evaluate which acquisition strategy is most suitable to reconstruct volumes with the presented approach, the trajectories for each acquisition type were compared based on the data obtained with the GE EM tracking system. Patient 1 and 2 were discounted from this analysis as the sonographers were still familiarizing themselves with the protocol when collecting data on them. Patient 4 was excluded because the GE EM tracking system was turned off for these examinations.

For each sweep, we manually reviewed the EM tracking data, removed inconsistent data with physically impossible position jumps, and selected the appropriate start time for the motion. The following two metrics were defined and computed as described to assess which sweeps are closest to a linear translation (results shown in Table 3.4):

Metric A – Rate of change in absolute deviation from start orientation [deg/sec]: For each time point, the absolute angle between the start pose and pose k was computed. The rate of change of these angles was then approximated by the slope of a first order polynomial fitted to the angle deviation data versus time. This angular velocity was then averaged for each type of acquisition sweep to obtain a metric to assess whether a sweep type is characterized by a high or low rotational component in probe motion.

Metric B – Euclidean distance from start to end position divided by position arc length [%]: This value equals 100 % for perfectly linear translation and decreases with decreasing nonlinearity in translation.

The presented data indicates that sweeps from the back are most suited to collect and register ultrasound volumes. This is in agreement with the sonographers' intuition. Limiting future patient visits for this ongoing study to these acquisitions will enable a significant reduction in exam time.

Table 3.4: Evaluation of different acquisition strategies

Probe position on body	Sweep direction relative to kidney	Number of sweeps evaluated	Metric A [deg/sec]		Metric B [%]	
			Mean	Standard deviation	Mean	Standard deviation
Lateral	Transverse	15	14.89	13.35	77.09	4.33
Lateral	Longitudinal	15	4.34	3.33	78.83	10.62
Lateral	Fan	12	19.50	4.28	48.67	19.47
Back	Transverse	16	12.89	4.79	83.39	4.06
Back	Longitudinal	14	0.95	0.99	88.53	2.05

3.4.3 Stability of Skin Features for Monocular Pose Estimation

The scarcity of highly distinct features on skin at the resolution of the selected camera makes monocular pose estimation from skin features challenging, even in ideal imaging conditions. As this effect is exacerbated by motion blur and the bad lighting conditions typically found in an ultrasound examination room, traditional corner and feature detectors did not work well on our data set of skin videos despite external light sources aimed at the patient's skin. We therefore chose to rely solely on the EM tracking data for the registration of the ultrasound images.

3.4.4 Selected Kidney Volumes from Ultrasound Scans

We computed selected kidney volumes using Stradwin (Version 5.2, available at http://mi.eng.cam.ac.uk/~rwp/stradwin; [69]), a tool for freehand 3D ultrasound measurement and visualization. The following analysis was limited to select scans, as the current method relies on extensive manual work and is thus not suited for the processing of more than 100 ultrasound videos with 50 – 100 frames each.

The scans were selected to for the availability of GE EM tracking data and their relatively translational acquisition motion (see also Section 3.4.2): only longitudinal scans recorded on the patients' backs were used for this analysis. The total out-of-plane displacement across each scan was obtained from the GE EM tracking data. The selected ultrasound scans were manually annotated and scaled appropriately. The resulting volumes are shown in Table 3.5. Figure 3.8 shows the visualization of two such volumes.

Table 3.5: Kidney volumes from ultrasound sweeps

Patient / kidney	Scan type	Volume estimate [ml]
Patient 2 / right	Back, longitudinal	105.042
Patient 2 / left	Back, longitudinal	112.527
Patient 3 / right	Back, longitudinal	121.206
Patient 3 / left	Back, longitudinal	118.097

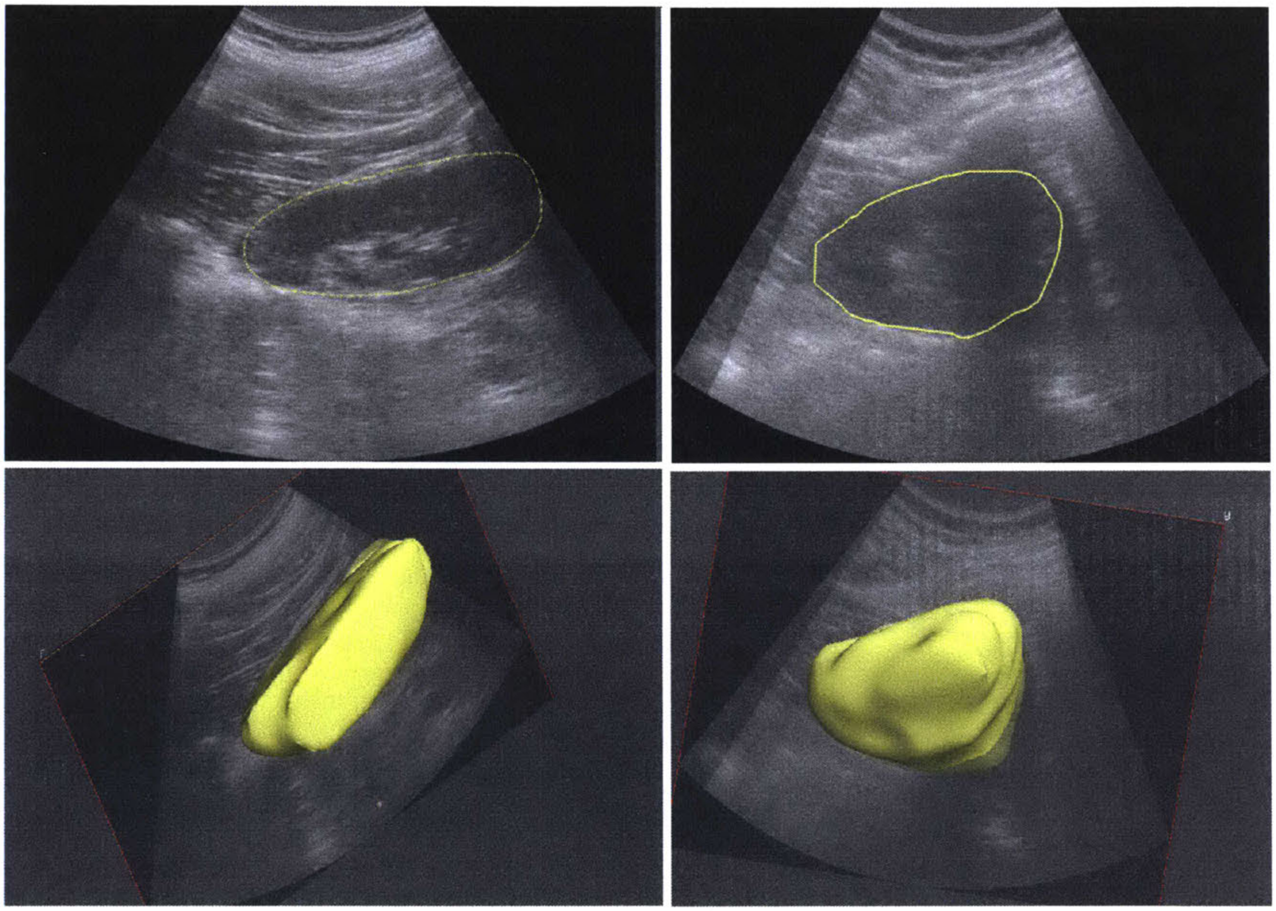

Figure 3.8: Visualization of manually annotated volumes of right kidney for patients 2 (left) and 3 (right)

3.4.5 Comparison of Kidney Volumes from CT and Ultrasound Scans

There is a consistent discrepancy between the kidney volumes obtained from CT scans and ultrasound sweeps respectively, with the values being measured in the CT scans being larger in all cases. With the exception of the measurement for patient 1, right kidney, all volumes from the CT scans are in agreement with values reported in literature (measured from MRI scans [70]). The volumes measured using ultrasound sweeps are slightly smaller than what has been reported for the sonographic quantification of kidney volumes [71]. The current ultrasound based volumetry seems to underestimate kidney volumes. This error likely stems from imprecisions in both the kidney annotations and the probe motion estimates.

3.4.6 Recommended Adjustments

Observing the sonographers acquiring data on multiple subjects in a clinical setting, frequent discussions with medical doctors, and a continuous review of the relevant literature have led to a number of conclusions on how to adjust our hardware and software to potentially achieve a higher accuracy. These insights and recommendations on how to adjust the probe design and the reconstruction algorithm are discussed below.

3.4.6.1 Camera placement

This section discusses how the camera should be oriented with respect to the ultrasound probe, particularly whether it should be mounted on the front (Figure 3.9, left) or side of the probe (Figure 3.9, right). The discussion considers (1) the sonographers ability to control for different aspects of the motion, (2) how the camera placement affects the tracking of skin features between frames (as required for pose estimation), and (3) how estimation errors in the different pose parameters propagate to affect the final volume estimate. This discussion refers to the probe axes as defined in Figure 3.10.

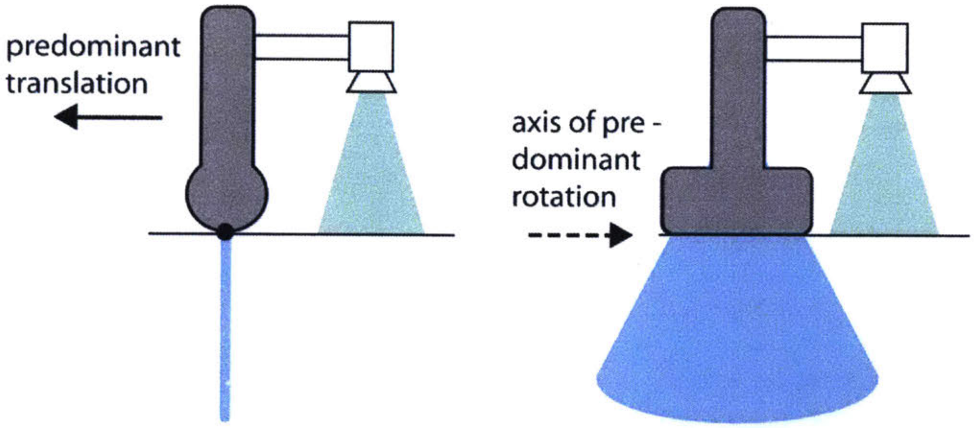

Figure 3.9: Camera placement on the front (left) and side (right) of the ultrasound probe

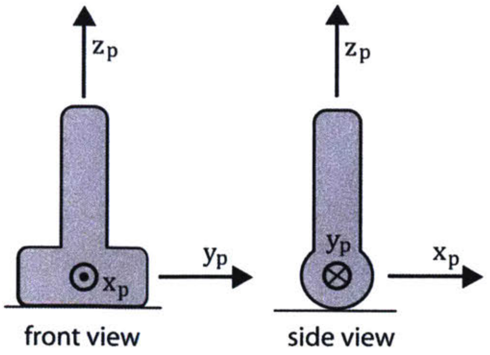

Figure 3.10: Probe coordinate system

(1): Sonographers receive good visual feedback from the ultrasound images on motion within the ultrasound imaging plane, i.e. translations along y_p and rotations around x_p. Unvoluntary motions in these directions are therefore less likely.

(2): Mounting the camera closer to z_P results in a smaller change in the camera image for a given rotation along the axis normal to the plane defined by z_P and the camera arm. This is qualitatively illustrated in Figure 3.11. A smaller change between subsequent camera images facilitates the reliable tracking of features.

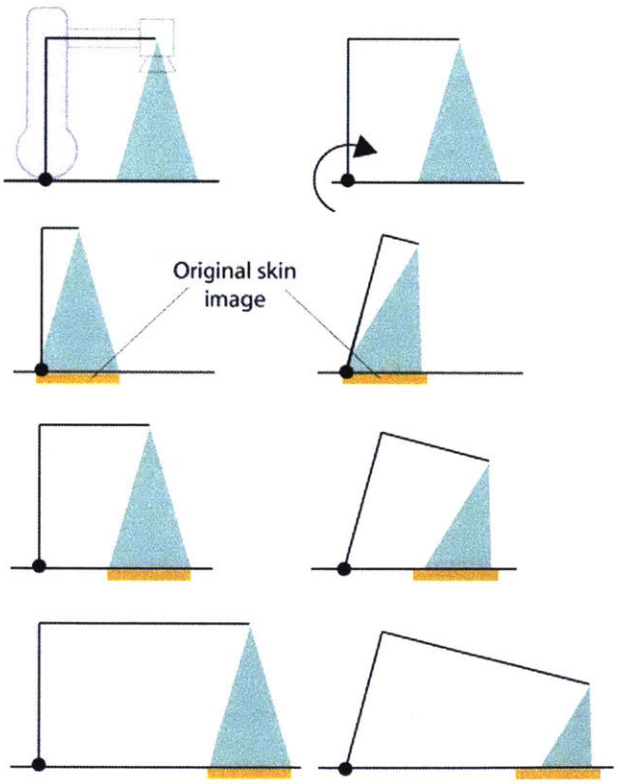

Figure 3.11: The offset between probe axis and camera affects the rate at which camera images change for a given rotation

(3): Errors in estimating different aspects of the pose differ in their effect on the final volume estimation error. The following simplified example, reduced from three to two dimensions, illustrates this concept. Consider the task of measuring the area of a rectangle by acquiring 1D lines across it (corresponding to the ultrasound images) while (inaccurately) measuring the acquisition pose of each line. For simplicity, the ground truth poses are assumed to be as shown in Figure 3.12 (top left). The poses are described by position (x, y) and orientation α. For $\alpha = 0$, wrongly estimating the pose with a rotational error α_e leads to an error in estimated area $A_{e\alpha}$, which can be calculated as

$$A_{e\alpha} = \frac{1}{2} L(h\,(\cos \beta\alpha_e - 1) + L \sin \beta\alpha_e),$$

or, for α_e small, approximated as

$$A_{e\alpha} \sim \frac{1}{2} L^2 \alpha_e.$$

It is straightforward to see that an error y_e in position estimate in the direction perpendicular to the imaging line (or plane in the 3D case), leads to an error in estimated area $A_{ey} = y_e L$ (Figure 3.12, bottom right). An error in position estimate in the direction of the imaging line (or plane), however, does not affect the estimate for A (Figure 3.12, bottom left). Similarly, volume estimates are likely to be less affected by pose estimation errors within the imaging plane (see also Cavalieri's Principle).

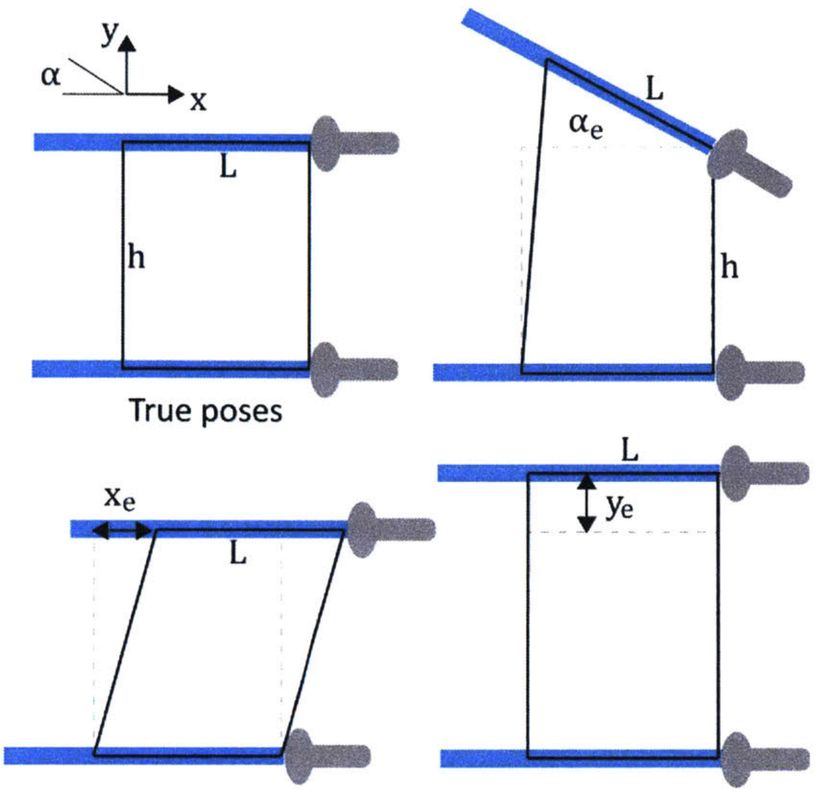

Figure 3.12: The effect of errors in pose estimation on the accuracy of volume estimation

The two camera mounting positions shown in Figure 3.9 have identical capabilities to detect rotations around z_P. Mounting the camera on the front (or side) allows for a higher accuracy in detecting rotations around x_P (or y_P respectively). Since rotations around y_P are both more likely to occur and more strongly affecting the volume estimate, it would be beneficial to adjust the design and mount the camera on the side of the probe as shown in Figure 3.9, right. In addition, ultrasound gel, which reduces the visibility of skin features and may cause glare, is less likely to accumulate on the side of the probe.

3.4.6.2 Depth estimation and scale

When estimating the location of a given feature in three-dimensional space based on its occurrence in a sequence of images acquired with a monocular camera, the estimation of depth is particularly challenging and the scale of a scene can only be recovered with appropriate initialization [72], [73]. Equipping mobile robots with laser range finders in addition to cameras was shown to improve their localization and mapping capabilities [74], [75]. Similarly, it may be beneficial to expand the hardware with a simple distance sensor placed on the front of the probe to measure the distance to the skin. This would also facilitate the detection of rotations around y_P, further increasing the accuracy of volume measurements. Such distance sensors are compact, low-cost, and cheap (e.g. Sharp GP2Y0A51SK0F, Sharp Microlectronics, WA).

3.4.6.3 Integration of Inertial Measurement Unit

Recent work has shown that errors in simultaneous localization and mapping can be drastically reduced by combining one or multiple cameras with inertial measurement units (IMUs), an approach referred to as visual-inertial odometry [73], [76]–[79]. Similar improvements could be achieved by equipping the probe with an IMU.

3.4.6.4 Mapping in deformable environments

Approaches to vision-based simultaneous localization and mapping for autonomous mobile robots mostly deal with either artificial indoor (e.g. [80]–[84]) and outdoor scenes (such as roads, cities, e.g. [85]–[87]), or, less frequently, natural outdoor scenes (e.g. [88], [89]). Traditionally, image features are considered to represent physical, rigid landmarks that are invariant in time. Accordingly, most algorithms have been developed for *static* environments [90].

Reconstructing a three-dimensional map of internal organs from ultrasound images and skin videos however requires the extraction, matching and registration of features on non-rigid structures in a scenario where the sensor (i.e. the ultrasound probe) actively interacts and deforms the observed scene. This introduces the additional requirement that the mapping algorithm is able to reason about scene deformation. Recently, initial approaches to tracking and reconstructing non-rigid have been demonstrated. Real-time fusion of non-rigidly deforming scenes has been achieved using an RGBD sensor (output: color image and depth map) [91]. Additionally, the simultaneous estimation of camera pose and non-rigid shape from monocular images was successfully applied to videos from a human back and face [92]–[94]. It would be invaluable to expand these approaches to improve the herein presented ultrasound volumetry.

3.5 Summary

The presented work successfully demonstrates the feasibility of measuring kidney volumes in a clinical setting using freehand ultrasound probes. However, multiple improvements to the data acquisition and processing are required to enable the reconstruction of more precise volumes (see Section 3.4.6 for a detailed discussion). A potential solution could be to introduce artificial skin features, similar to the demonstration of checkerboard-based pose estimation demonstrated in Chapter 4.

Furthermore, the current approach relies on the laborious manual segmentation of the ultrasound images. A method to identify tissue interfaces in ultrasound images and propagate them though a volume sweep has been presented as a first step towards partially automating the kidney segmentation.

CHAPTER

4

TOWARDS FORCE-CONTROLLED ULTRASOUND VOLUME ELASTOGRAMS

The following chapter presents the acquisition and evaluation of initial force-correlated ultrasound volume elastograms. These elastograms were acquired on phantoms by mounting an ultrasound probe on a CNC stage to decouple this conceptual demonstration from uncertainties in pose estimation that stem from reconstructing the probe motion by either tracking features in the camera images or using an electromagnetic pose tracking system as described in Section 3.3.2.2.

4.1 Materials and Methods

4.1.1 Experimental Set-up

The imaging hardware used in these experiments was identical to the system described in Section 2.1.1.1. Its shear wave imaging feature for the Philips C5-1 probe enables the acquisition of 2D in-frame elasticity maps in an adjustable region of interest (significantly smaller than the size of the B-Mode image). This elasticity map is then overlaid on top of a B-mode image and the resulting image is displayed next to the unmodified B-mode image.

The probe shell (housing the ultrasound probe and a load-cell as described in Section 2.1.1.2) was modified such that it can be mounted to a CNC stage with three translational degrees of freedom (see Figure 4.1). The motion along each axis of the stage was controlled through a stepper motor driving a lead screw. A LabVIEW (National Instruments) program was run in real-time on an NI myRIO (National Instruments) to allow for an automatically controlled probe preload relying on a feedback loop to adjust the probes z-position based on the error between desired and measured force.

A checkerboard pattern was rigidly mounted on the imaging target such that it is in full view of the camera throughout all acquisition positions (see Figure 4.2).

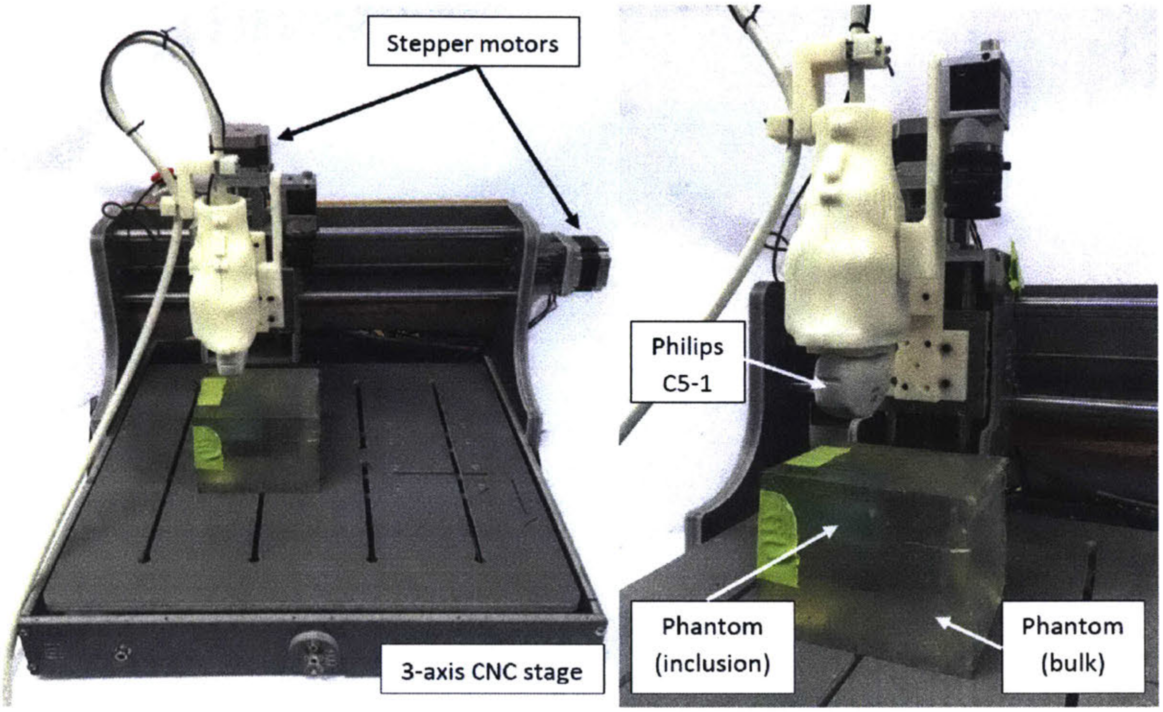

Figure 4.1: CNC stage with custom probe mount for the acquisition of linear ultrasound sweeps with controlled preload

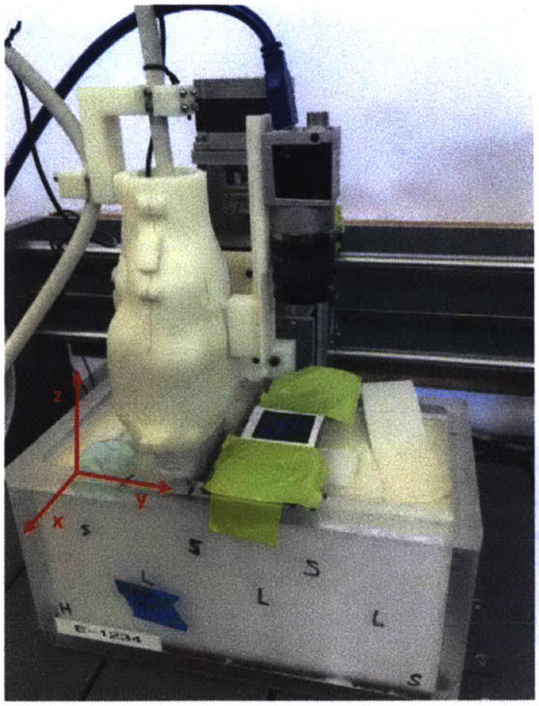

Figure 4.2: Setup for force-correlated volume elastograms including checkerboard pattern for visual position tracking

4.1.2 Imaging Target

Initial data was taken on a custom phantom (shown in Figure 4.1), which was made to contain an inclusion of decreased stiffness relative to the bulk material. The bulk material was made from Kraton ThermoRubber Copolymer (Kraton, Houston, TX) and Clarion White Mineral Oil Food Grade 90 (Clarion Lubricants, Houston, TX) according to the protocol in Appendix A.2 (adapted from [95]). A cylindrical hole was incorporated into the bulk material during the molding process and later filled with ultrasound gel (Aquasonic 100 Ultrasound Transmission Gel, Parker Laboratories, Inc., Fairfield, NJ) to serve as a low-stiffness inclusion.

Additional data was taken on a phantom containing inclusions of increased stiffness (phantom obtained from Philips Research, shown in Figure 4.2). This phantom contained spherical inclusions of varying stiffness (stiff, very stiff), size (small, large), and depth (shallow, deep). Volume elastographs were taken of the small, shallow inclusion labeled as stiff.

4.1.3 Data Acquisition Protocols

Images from the camera and ultrasound stream were captured simultaneously for a number of probe motions across the imaging target as described in Sections 4.1.3.1 to 4.1.3.3. If not denoted differently, the acquisitions were started before the imaged inclusion and stopped after the probe had passed it. The camera was placed to film a tag with known features to simplify reconstructing the probe motion from the stream of camera images.

4.1.3.1 Motor-Controlled Translation

Ultrasound and camera images were acquired for pure translational trajectories, relying on the CNC-stage described in 4.1.1 to control preload and probe pose. Acquisition sweeps were taken with preloads of 1 N, 2 N, 3 N and 6 N. For each of those sweeps, the probe was moved perpendicular to the ultrasound imaging plane (y-axis in Figure 4.2) and images were captured with a linear displacement of 2 mm between acquisitions. As the accuracy of the ultrasound imager's shear wave elastography feature is negatively impacted by motion, the probe was held in place for at least 10 s at each acquisition position before the data was captured.

4.1.3.2 Motor-Controlled Force-Sweep

A force sweep, i.e. slowly increasing the preload force with constant probe position (except variation in height, see z-axis in Figure 4.2), was acquired with the probe placed above the center of the inclusion. The preload was increased from 1 N to 10 N in 1 N increments. The probe was held in place for at least 10 s at each acquisition position before the data was captured for increased accuracy.

4.1.3.3 Freehand Translation

A manual sweep of the inclusion was conducted to as a preliminary step towards force-correlated ultrasound volume elastograms with a hand-held probe. The probe was held in place for at least 10 s at each acquisition position before the data was captured for increased accuracy. The operator put high effort in trying to manually restrict the probe motion to a translation perpendicular to the ultrasound plane (i.e. along the global z-axis).

4.1.4 Pose Inference

For each of the acquisitions outlined in Section 4.1.3, the following approaches were used independently to infer pose:

- ground truth from CNC stage motion (if available)
- Pose from tracking a checkerboard pattern (rigidly mounted to phantom), filmed with the camera. OpenCV's [96] implementation of the PnP algorithm was used to compute the motion of the checkerboard pattern between frames.

4.2 Results

Due to the limited resolution of the implemented approach to shear wave elastography, it was impossible to distinguish the low-stiffness inclusion in the custom made phantom containing ultrasound gel. In the following, only the results on the phantom containing inclusions of increased stiffness are reported.

An exemplary snap shot of the collected image streams (camera images of a tag and ultrasound B-mode image with tissue stiffness map) is shown in Figure 4.3. The elasticity maps presented in the following were cropped out of the respective ultrasound frame for better visualization.

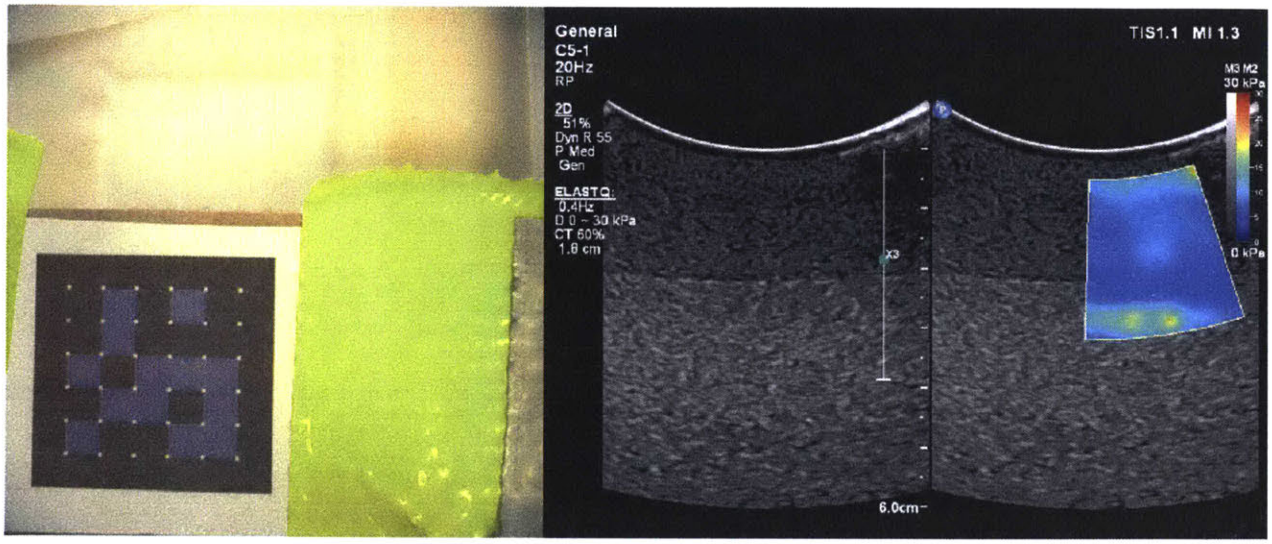

Figure 4.3: Camera and ultrasound image stream as collected with the volume elastography setup

4.2.1 Motor-Controlled Translation

Figure 4.4 shows the probe poses for all preloads reconstructed as described in Section 4.1.4 (projected on the xy- and yz-plane respectively; all trajectories start at height z = 0, offset introduced in z-direction for readability). Figure 4.5 shows a visualization of the volume elastogram for 1 N assuming perfectly linear translation for the probe motion and the uncropped B-mode and elastography images for 20 mm translation (mid-inclusion) are shown in Figure 4.6. Figure 4.7 shows the same three-dimensional visualization of the stiffness map for the sweep with a preload of 6 N.

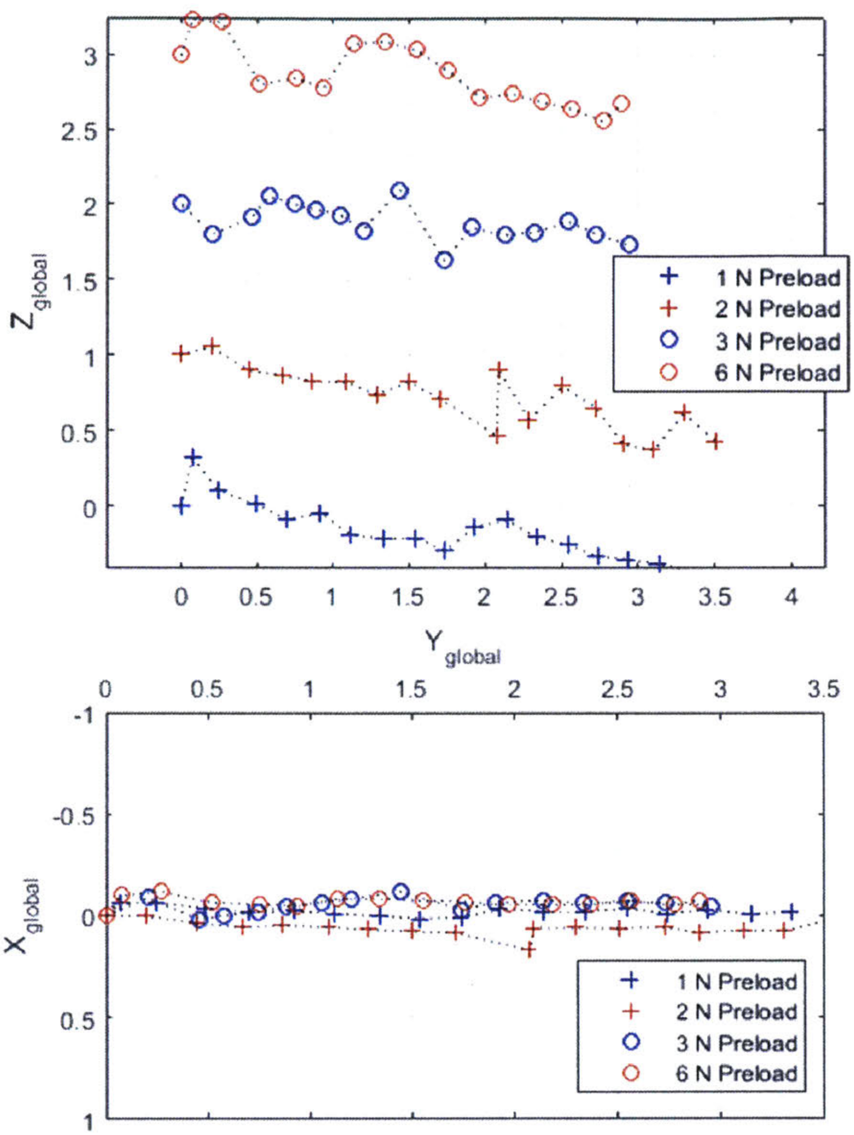

Figure 4.4: Probe poses as reconstructed for the guided sweeps from the camera image containing the fixed checkerboard

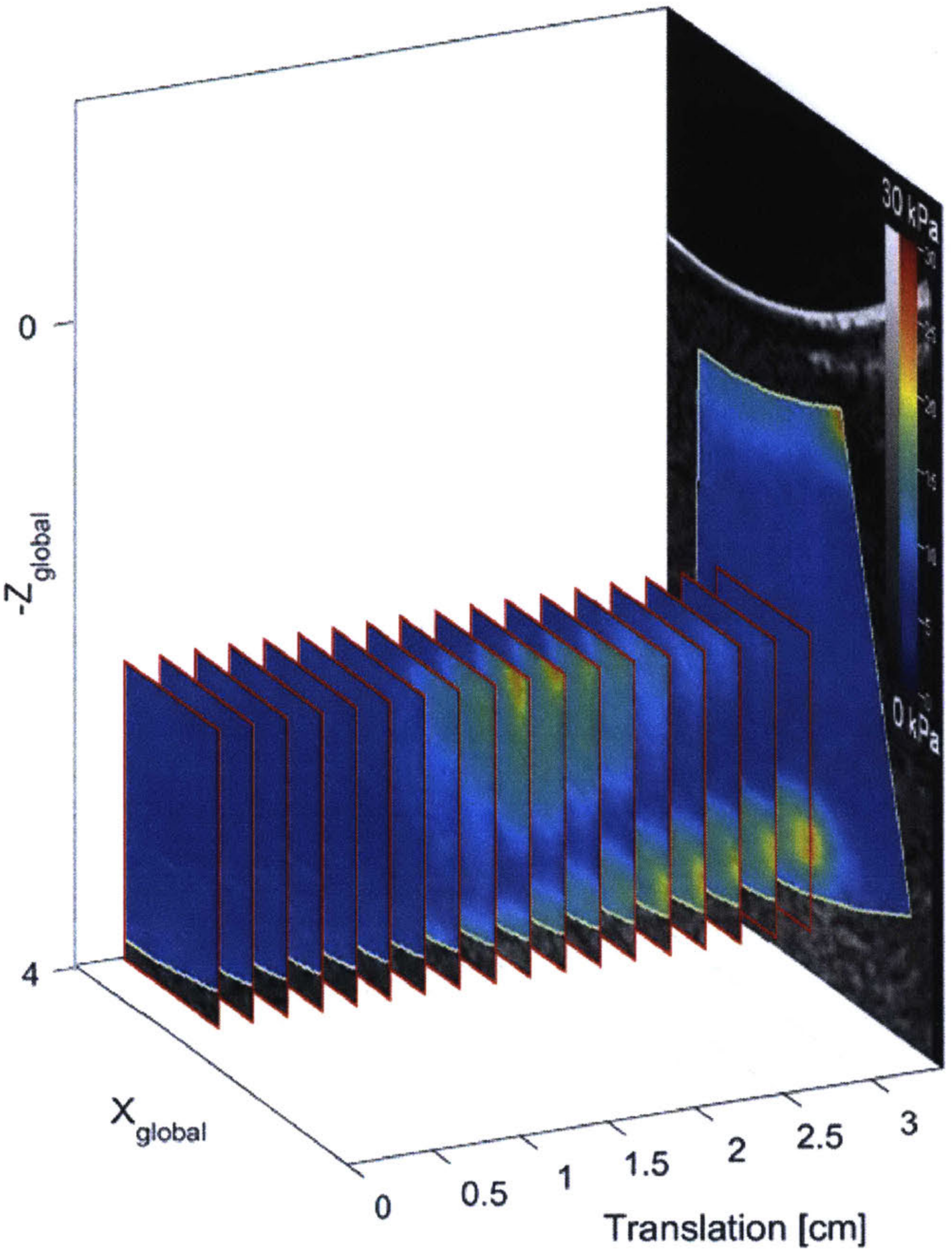

Figure 4.5: Visualization of volume elastogram acquired with 1 N preload

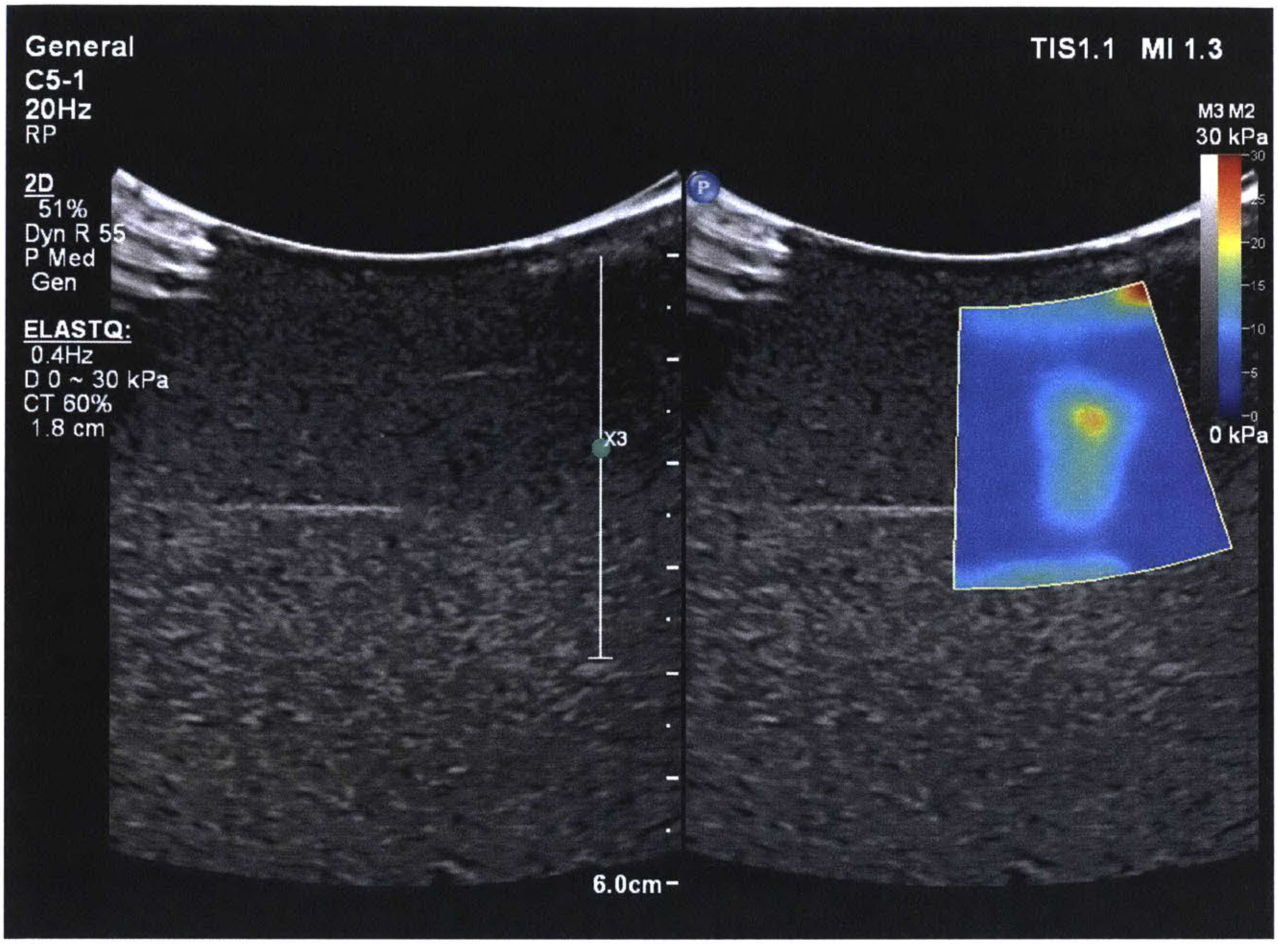

Figure 4.6: Comparison of B-mode image and shear wave elasticity map of the inclusion taken at 1 N preload

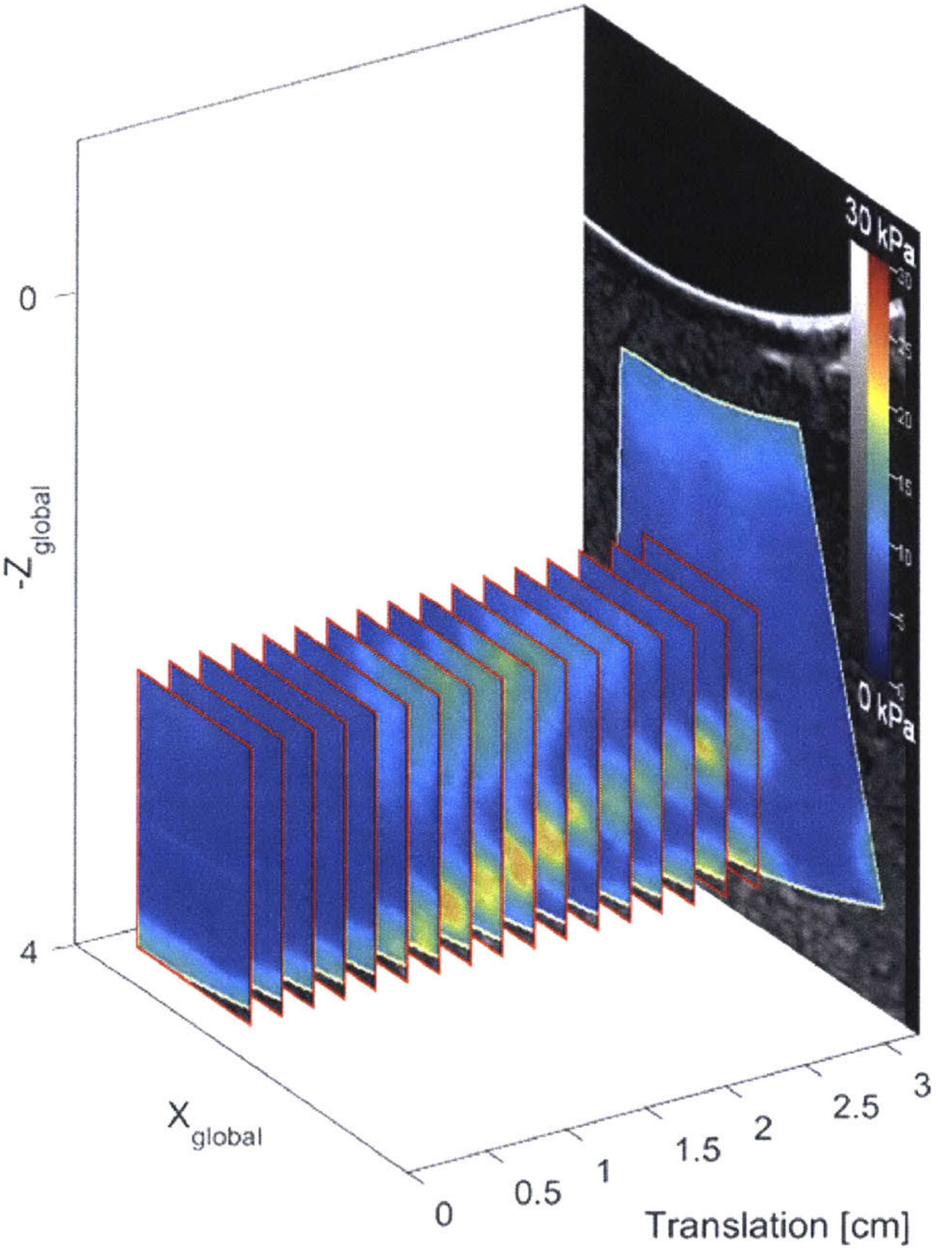

Figure 4.7: Visualization of volume elastogram acquired with 6 N preload

4.2.2 Motor-Controlled Force-Sweep

Figure 4.8 shows the elastography maps of the inclusion surrounded by bulk phantom material at different preloads.

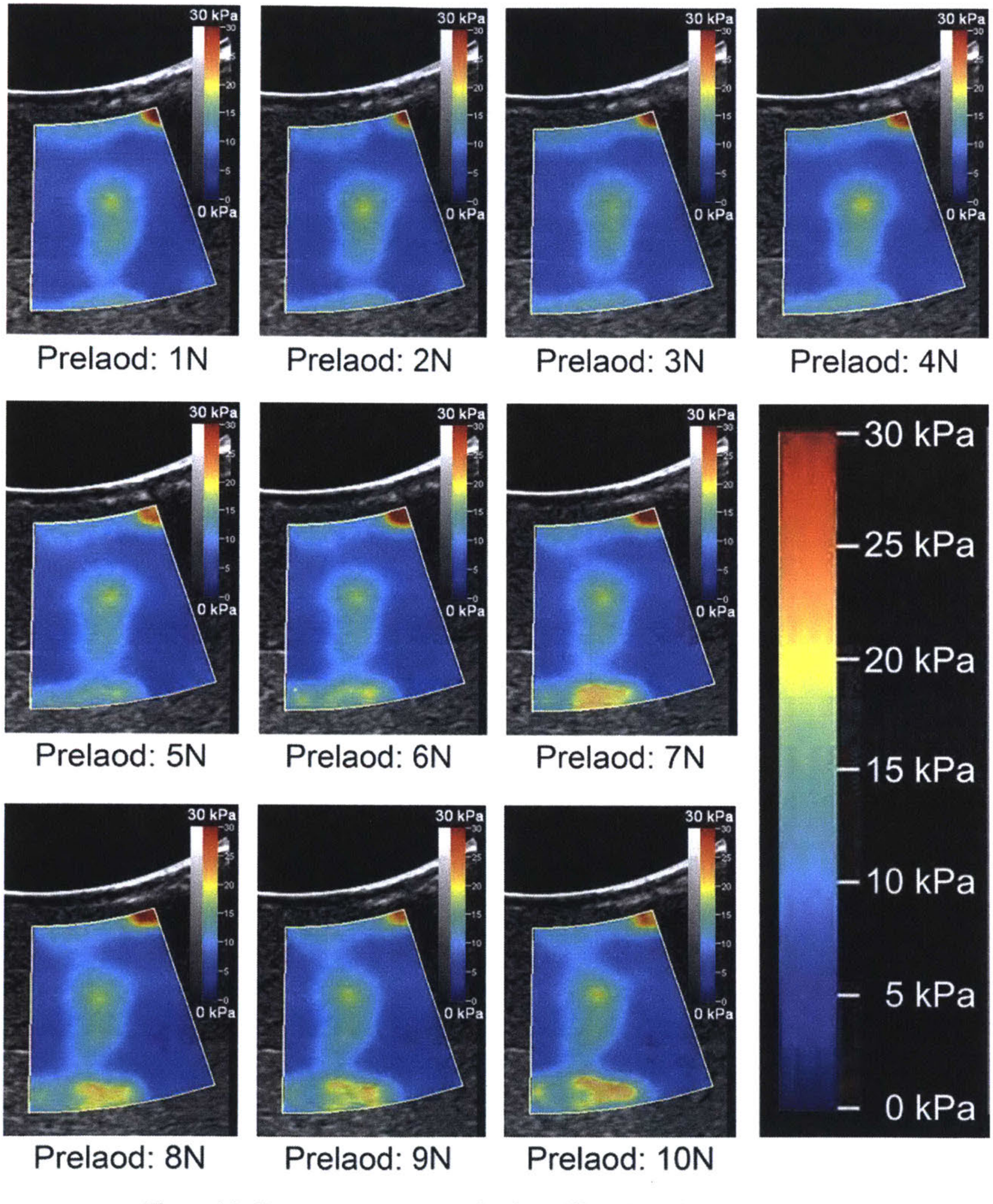

Prelaod: 1N Prelaod: 2N Prelaod: 3N Prelaod: 4N

Prelaod: 5N Prelaod: 6N Prelaod: 7N

Prelaod: 8N Prelaod: 9N Prelaod: 10N

Figure 4.8: Shear wave elastogram of a high stiffness inclusion versus preload

4.2.3 Freehand Translation

Figure 4.9 shows a visualization of the relative positions of the ultrasound frames in the freehand acquisition, reconstructed as described in Section 4.1.4. Figure 4.10 shows a sliced, cropped stack of the acquired elasticity maps, (wrongly) assuming linear probe motion.

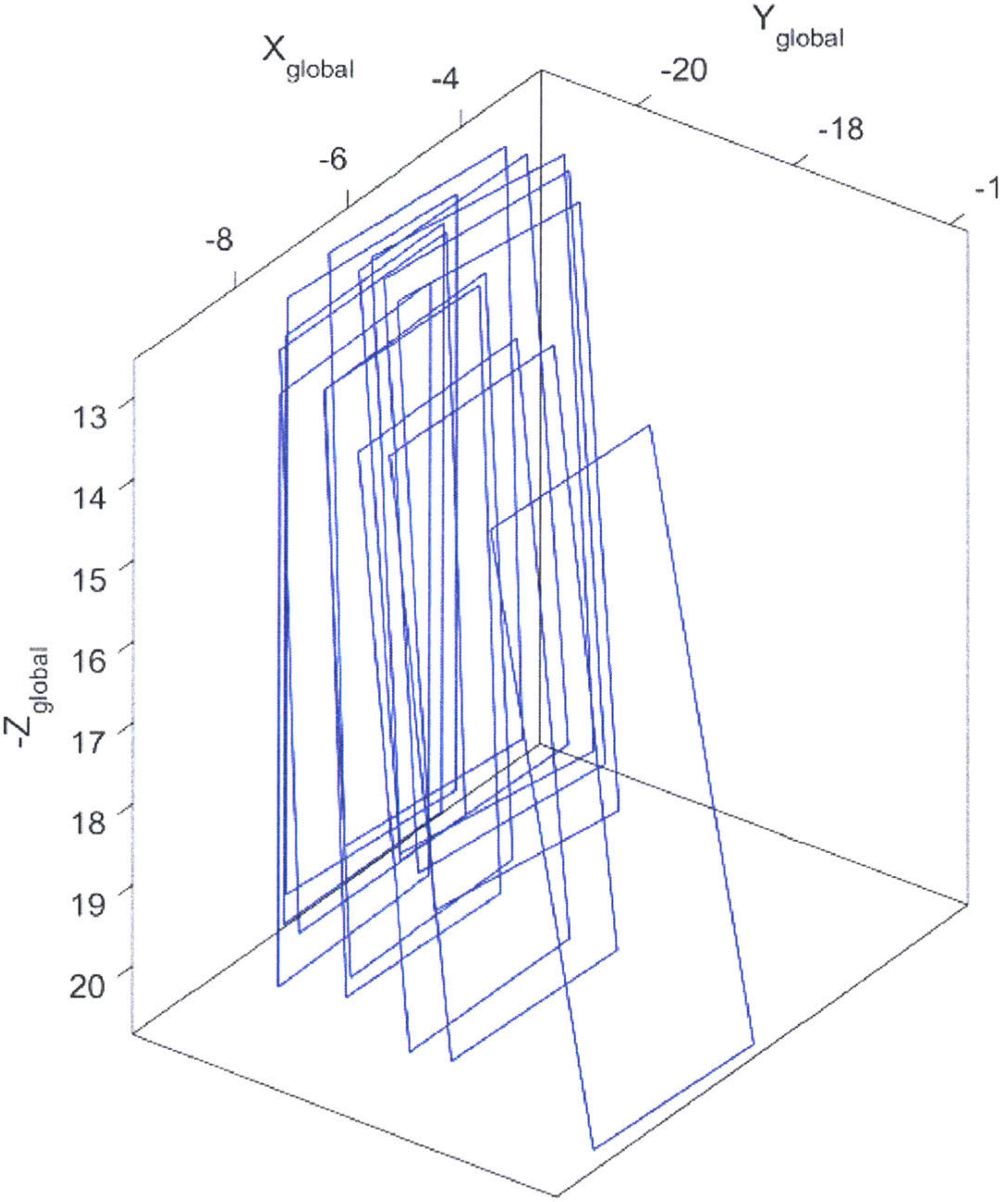

Figure 4.9: Visualization of ultrasound frame positions during freehand acquisition of volume elastograms

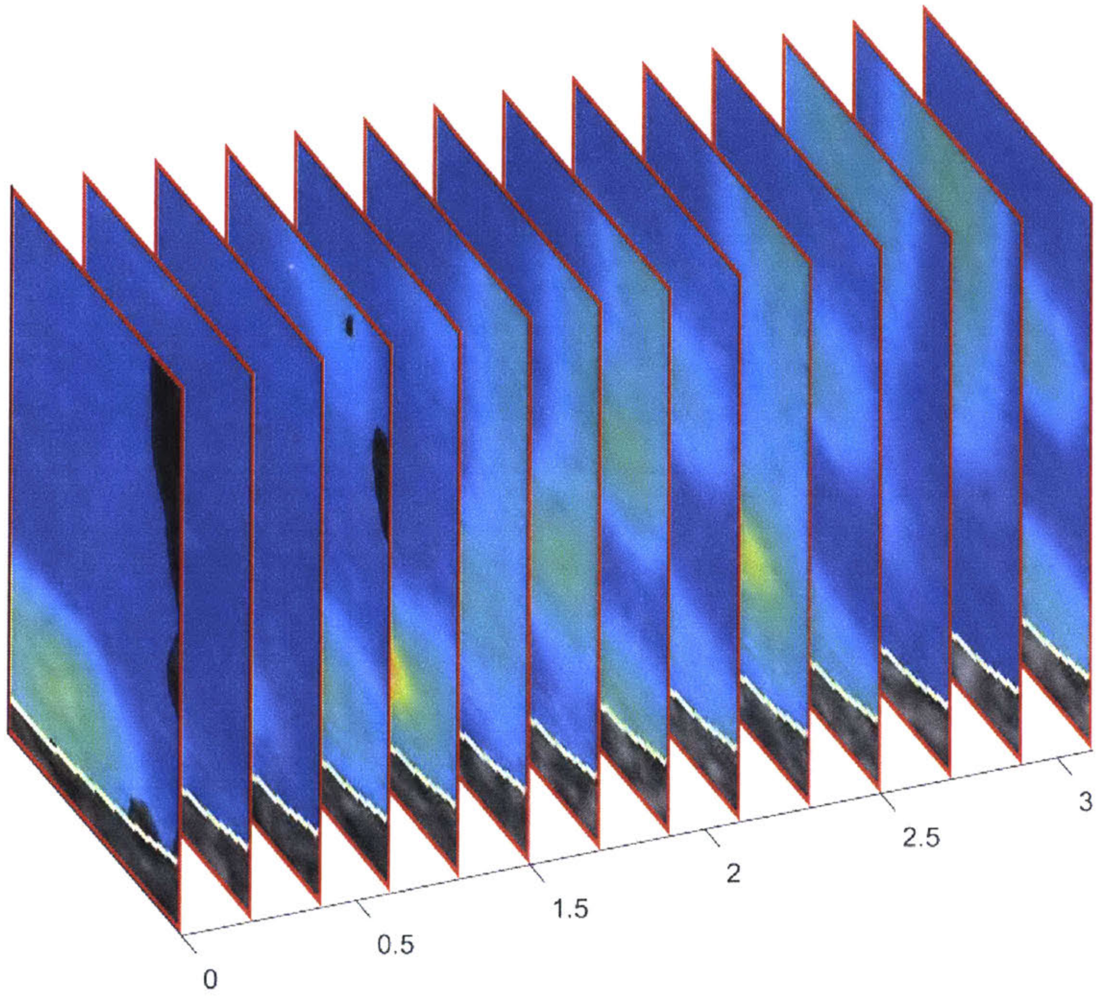

Figure 4.10: Cropped stiffness maps from freehand acquisition of volume elastograms

4.3 Discussion

A successful demonstration of ultrasound-based force-correlated volume elastography was demonstrated. In particular, a high-stiffness inclusion in a phantom was successfully identified and localized in space through shear wave imaging (see Figure 4.11) with guided ultrasound probe motion. It is worth noting that this artificial lesion does not show up in the traditional B-Mode images. The additional high stiffness region (see Figure 4.11) identified below the depth of the inclusion likely stems from damages in the phantom due to aging and frequent use under high compressive loads.

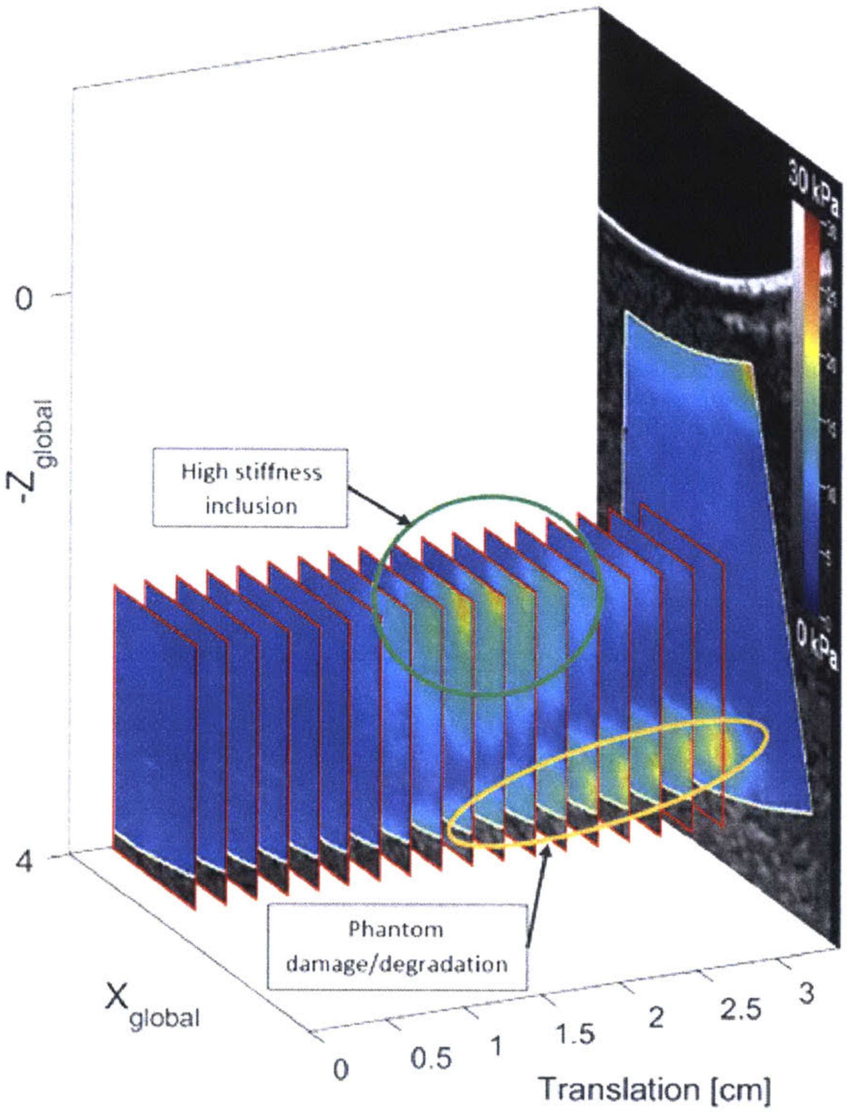

Figure 4.11: Annotated volume elastogram acquired with 1 N preload

The standard deviations in camera position (global x- and z-axis) for each of the guided linear sweeps are listed in Table 4.1. Assuming a purely linear motion along the global y-axis, these should be zero in the case of perfect translation and perfect position measurement. The variations in the measured z-coordinate are consistently larger. This effect can be attributed to the known challenge of estimating the depth of observed features in monocular vision.

Table 4.1: Variation in probe position reconstructed from camera vision

Acquisition description	Standard deviation of position	
	along x-axis [cm]	along z-axis [cm]
CNC, 1 N Preload	0.0222	0.1891
CNC, 2 N Preload	0.0368	0.2063
CNC, 3 N Preload	0.0364	0.1245
CNC, 6 N Preload	0.0263	0.2104

No significant difference in measured elasticity can be identified for varying preloads. This is as expected for a linearly elastic phantom and in agreement with the findings reported in Section 2. However, a strong dependence of the measured stiffness on preload is expected for ex- and in-vivo tissue, similar to the effect observed in the experiments on the force-dependence of local stiffness measurements in ex-vivo tissue (see Section 2).

Several improvements are required in order to enable a high quality reconstruction of volume elastograms from freehand acquisitions in a clinical setting. Key steps are an improved estimation of the probe pose using artificial and natural skin features; an acceleration of the implemented shear wave elastography; and the development of a method to reduce the large negative impact of motion on the accuracy of the shear wave based stiffness estimates.

CHAPTER

5

CONCLUSIONS AND OUTLOOK

This work presents data on the preload dependence of shear wave elastography in biological tissue, initial results on an ongoing clinical study on using ultrasound for kidney volumetry, and the first demonstration of force-correlated volume elastography.

The observed strain hardening in biological tissue motivates the assessments of preload dependence on ultrasound elastography in a human subject study in clinically relevant target tissue such as breast or thyroid. It would be particularly insightful to use the presented probe to extract and compare the strain hardening rate from both healthy and diseased tissue. These findings further highlight the importance to control for variations in preload when basing diagnosis on ultrasound-based elasticity measurements to achieve an improved repeatability.

The findings from the ongoing clinical study on renal volumetry demonstrate the method's potential to quantify clinically relevant volumes (e.g. organs and muscles). The data on probe pose collected in a total of 89 acquisition sweeps on 3 patients allowed for the identification of an ideal image acquisition strategy for ultrasound-based kidney volumetry. Together with minor practical adjustments made after repeatedly observing the clinician's use of the technology, this will significantly facilitate and accelerate future data collection.

The application of force-correlated volume elastography to the identification of an inclusion with increased stiffness, invisible in traditional B-mode imaging, highlights the potential of this concept to provide a quantitative alternative to manual palpation. However, additional experiments are required to determine the spatial resolution of the method.

Using the experimental setup with the CNC stage for position and preload control, we will collect force-correlated volume elastograms of ex-vivo tissue. Ideally, these samples would contain pathological and healthy tissue. It would also be interesting to acquire force-correlated volume elastograms of muscles in healthy human volunteers, and try to link them to their performance. Future work will further aim to combine shear wave elastography with the capabilities of preload control and pose-estimation through a probe-mounted camera in a hand-held device. While this requires advances in both the pose estimation and the shear wave elastography (mainly in frame rate and reliability), such a probe could be invaluable in many clinical scenarios, ranging from precisely assessing the size of breast or thyroid nodules, to staging NAFLD with increased reproducibility compared to localized methods, to predicting malignancy of cancer lesions. It could further lead to an improvement in these procedures by providing a measure of tissue non-linearity, which has the potential to serve as an additional property that facilitates the distinction between healthy and diseased tissue.

REFERENCES

[1] J. Bamber, D. Cosgrove, C. F. Dietrich, J. Fromageau, J. Bojunga, F. Calliada, V. Cantisani, J. Correas, M. D'Onofrio, E. E. Drakonaki, M. Fink, M. Friedrich-Rust, O. H. Gilja, R. F. Havre, C. Jenssen, A. S. Klauser, R. Ohlinger, A. Saftoiu, F. Schaefer, I. Sporea, and F. Piscaglia, "EFSUMB guidelines and recommendations on the clinical use of ultrasound elastography. Part 1: Basic principles and technology.," *Ultraschall Med.*, vol. 34, no. 2, pp. 169–84, 2013.

[2] P. S. Wellman, R. D. Howe, E. Dalton, and K. A. Kern, "Breast Tissue Stiffness in Compression is Correlated to Histological Diagnosis."

[3] M. Yoneda, M. Yoneda, H. Mawatari, K. Fujita, H. Endo, H. Iida, Y. Nozaki, K. Yonemitsu, T. Higurashi, H. Takahashi, N. Kobayashi, H. Kirikoshi, Y. Abe, M. Inamori, K. Kubota, S. Saito, M. Tamano, H. Hiraishi, S. Maeyama, N. Yamaguchi, S. Togo, and A. Nakajima, "Noninvasive assessment of liver fibrosis by measurement of stiffness in patients with nonalcoholic fatty liver disease (NAFLD)," *Dig. Liver Dis.*, vol. 40, no. 5, pp. 371–378, 2008.

[4] V. W.-S. Wong, J. Vergniol, G. L.-H. Wong, J. Foucher, H. L.-Y. Chan, B. Le Bail, P. C.-L. Choi, M. Kowo, A. W.-H. Chan, W. Merrouche, J. J.-Y. Sung, and V. de Lédinghen, "Diagnosis of fibrosis and cirrhosis using liver stiffness measurement in nonalcoholic fatty liver disease.," *Hepatology*, vol. 51, no. 2, pp. 454–62, 2010.

[5] M. Friedrich-Rust, M.-F. Ong, S. Martens, C. Sarrazin, J. Bojunga, S. Zeuzem, and E. Herrmann, "Performance of transient elastography for the staging of liver fibrosis: a meta-analysis.," *Gastroenterology*, vol. 134, no. 4, pp. 960–74, Apr. 2008.

[6] D. S. Cooper, G. M. Doherty, B. R. Haugen, B. R. Hauger, R. T. Kloos, S. L. Lee, S. J. Mandel, E. L. Mazzaferri, B. McIver, F. Pacini, M. Schlumberger, S. I. Sherman, D. L. Steward, and R. M. Tuttle, "Revised American Thyroid Association management guidelines for patients with thyroid nodules and differentiated thyroid cancer.," *Thyroid*, vol. 19, no. 11, pp. 1167–214, Nov. 2009.

[7] Z. Huang, J. Zheng, J. Zeng, X. Wang, T. Wu, and R. Zheng, "Normal Liver Stiffness in Healthy Adults Assessed By Real-Time Shear Wave Elastography and Factors That

Influence This Method," *Ultrasound Med. Biol.*, vol. 40, no. 11, pp. 2549–2555, 2014.

[8] M. Etzel, C. Happel, F. von Müller, H. Ackermann, J. Bojunga, and F. Grünwald, "[Palpation and elastography of thyroid nodules in comparison].," *Nuklearmedizin.*, vol. 52, no. 3, pp. 97–100, 2013.

[9] P. Albers, W. Albrecht, F. Algaba, C. Bokemeyer, G. Cohn-Cedermark, A. Horwich, O. Klepp, M. P. Laguna, and G. Pizzocaro, "Guidelines on Testicular Cancer," *Eur. Urol.*, vol. 48, no. 6, pp. 885–894, Dec. 2005.

[10] M. Reiman, C. Burgi, E. Strube, K. Prue, K. Ray, A. Elliott, and A. Goode, "The utility of clinical measures for the diagnosis of Achilles tendon injuries: A systematic review with meta-analysis," *J. Athl. Train.*, vol. 49, no. 6, pp. 820–829, 2014.

[11] S. M. Khoddami, N. N. Ansari, and S. Jalaie, "Review on Laryngeal Palpation Methods in Muscle Tension Dysphonia: Validity and Reliability Issues," *J. Voice*, vol. 29, no. 4, pp. 459–468, 2015.

[12] J. J. Hebert, S. L. Koppenhaver, D. S. Teyhen, B. F. Walker, and J. M. Fritz, "The evaluation of lumbar multifidus muscle function via palpation: Reliability and validity of a new clinical test," *Spine J.*, vol. 15, no. 6, pp. 1196–1202, 2015.

[13] J. W. Stockstill, A. J. Gross, and W. D. J. McCall, "Interrater reliability in masticatory muscle palpation.," *J. Craniomandib. Disord.*, vol. 3, no. 3, pp. 143–146, 1989.

[14] J. Yang, V. Schnadig, R. Logrono, and P. G. Wasserman, "Fine-needle aspiration of thyroid nodules: a study of 4703 patients with histologic and clinical correlations.," *Cancer*, vol. 111, no. 5, pp. 306–315, 2007.

[15] D. Saslow, C. Boetes, W. Burke, S. Harms, M. O. Leach, C. D. Lehman, E. Morris, E. Pisano, M. Schnall, S. Sener, R. A. Smith, E. Warner, M. Yaffe, K. S. Andrews, and C. A. Russell, "American Cancer Society guidelines for breast screening with MRI as an adjunct to mammography," *CA Cancer J Clin*, vol. 57, no. 2, pp. 75–89, 2007.

[16] T. M. Kolb, J. Lichy, and J. H. Newhouse, "Comparison of the Performance of Screening Mammography, Physical Examination, and Breast US and Evaluation of Factors that Influence Them: An Analysis of 27,825 Patient Evaluations," *Radiology*, vol. 225, no. 1, pp. 165–175, 2002.

[17] J. P. Kösters and P. C. Gøtzsche, "Regular self-examination or clinical examination for early detection of breast cancer.," *Cochrane database Syst. Rev.*, no. 2, p. CD003373, 2003.

[18] C. D. Williams, J. Stengel, M. I. Asike, D. M. Torres, J. Shaw, M. Contreras, C. L. Landt, and S. A. Harrison, "Prevalence of nonalcoholic fatty liver disease and nonalcoholic steatohepatitis among a largely middle-aged population utilizing ultrasound and liver biopsy: A prospective study," *Gastroenterology*, vol. 140, no. 1, pp. 124–131, 2011.

[19] M. E. Rinella, "Nonalcoholic fatty liver disease: a systematic review.," *JAMA*, vol. 313, no. 22, pp. 2263–73, 2015.

[20] S. M. Abd El-Kader and E. M. S. El-Den Ashmawy, "Non-alcoholic fatty liver disease: The diagnosis and management," *World J. Hepatol.*, vol. 7, no. 6, pp. 846–858, 2015.

[21] S. McPherson, T. Hardy, E. Henderson, A. D. Burt, C. P. Day, and Q. M. Anstee, "Evidence of NAFLD progression from steatosis to fibrosing-steatohepatitis using paired biopsies: Implications for prognosis and clinical management," *J. Hepatol.*, vol. 62, no. 5, pp. 1148–1155, 2015.

[22] P. Angulo, J. M. Hui, G. Marchesini, E. Bugianesi, J. George, G. C. Farrell, F. Enders, S. Saksena, A. D. Burt, J. P. Bida, K. Lindor, S. O. Sanderson, M. Lenzi, L. A. Adams, J. Kench, T. M. Therneau, and C. P. Day, "The NAFLD fibrosis score: A noninvasive system that identifies liver fibrosis in patients with NAFLD," *Hepatology*, vol. 45, no. 4, pp. 846–854, 2007.

[23] S. H. Caldwell, D. H. Oelsner, J. C. Iezzoni, E. E. Hespenheide, E. H. Battle, and C. J. Driscoll, "Cryptogenic cirrhosis: clinical characterization and risk factors for underlying disease.," *Hepatology*, vol. 29, no. 3, pp. 664–669, 1999.

[24] E. Bugianesi, N. Leone, E. Vanni, G. Marchesini, F. Brunello, P. Carucci, A. Musso, P. De Paolis, L. Capussotti, and M. Salizzoni, "Expanding the natural history of nonalcoholic steatohepatitis: From cryptogenic cirrhosis to hepatocellular carcinoma," *Gastroenterology*, vol. 123, no. 1, pp. 134–140, 2002.

[25] L. A. Adams, J. F. Lymp, J. St. Sauver, S. O. Sanderson, K. D. Lindor, A. Feldstein, and P. Angulo, "The natural history of nonalcoholic fatty liver disease: A population-based cohort study," *Gastroenterology*, vol. 129, no. 1. pp. 113–121, 2005.

[26] A. J. Sanyal, C. Banas, C. Sargeant, V. A. Luketic, R. K. Sterling, R. T. Stravitz, M. L. Shiffman, D. Heuman, A. Coterrell, R. A. Fisher, M. J. Contos, and A. S. Mills, "Similarities and differences in outcomes of cirrhosis due to nonalcoholic steatohepatitis and hepatitis C," *Hepatology*, vol. 43, no. 4, pp. 682–689, 2006.

[27] V. Ratziu, F. Charlotte, A. Heurtier, S. Gombert, P. Giral, E. Bruckert, A. Grimaldi, F. Capron, and T. Poynard, "Sampling variability of liver biopsy in nonalcoholic fatty liver disease," *Gastroenterology*, vol. 128, no. 7, pp. 1898–1906, 2005.

[28] D. J. Janiec, E. R. Jacobson, A. Freeth, L. Spaulding, and H. Blaszyk, "Histologic variation of grade and stage of non-alcoholic fatty liver disease in liver biopsies," *Obes. Surg.*, vol. 15, no. 4, pp. 497–501, 2005.

[29] J. L. Gennisson, T. Deffieux, M. Fink, and M. Tanter, "Ultrasound elastography: Principles and techniques," *Diagn. Interv. Imaging*, vol. 94, no. 5, pp. 487–495, 2013.

[30] U. Zaleska-Dorobisz, K. Kaczorowski, A. Pawlu??, A. Puchalska, and M. Inglot, "Ultrasound elastography - review of techniques and its clinical applications.," *Adv. Clin. Exp. Med.*, vol. 23, no. 4, pp. 645–655, 2014.

[31] R. J. Dewall, "Ultrasound elastography: principles, techniques, and clinical applications.," *Crit. Rev. Biomed. Eng.*, vol. 41, no. 1, pp. 1–19, 2013.

[32] A. Fenster, C. Blake, I. Gyacskov, A. Landry, and J. D. Spence, "3D ultrasound analysis of carotid plaque volume and surface morphology," *Ultrasonics*, vol. 44, no. SUPPL., 2006.

[33] C. D. Ainsworth, C. C. Blake, A. Tamayo, V. Beletsky, A. Fenster, and J. D. Spence, "3D ultrasound measurement of change in carotid plaque volume: A tool for rapid evaluation of new therapies," *Stroke*, vol. 36, no. 9, pp. 1904–1909, 2005.

[34] Z. Wei, G. Wan, L. Gardi, G. Mills, D. Downey, and A. Fenster, "Robot-assisted 3D-TRUS guided prostate brachytherapy: system integration and validation.," *Med. Phys.*, vol. 31, no. 3, pp. 539–548, 2004.

[35] T. M. Peters, "Image-guidance for surgical procedures.," *Phys. Med. Biol.*, vol. 51, no. 14, pp. R505–R540, 2006.

[36] W. E. Webler and M. S. Buhr, "Automated longitudinal position translator for ultrasonic imaging probes, and methods of using same," US5485846 A, 1996.

[37] R. J. Solomon, M. K. Mason, G. Gruner, and J. T. Fearnside, "Transducer positioning system," US5181514 A, 1993.

[38] V. Mor-Avi, L. Sugeng, L. Weinert, P. MacEneaney, E. G. Caiani, R. Koch, I. S. Salgo, and R. M. Lang, "Fast measurement of left ventricular mass with real-time three-dimensional echocardiography: comparison with magnetic resonance imaging.," *Circulation*, vol. 110, no. 13, pp. 1814–8, Sep. 2004.

[39] D. G. Gobbi, R. M. Comeau, and T. M. Peters, "Ultrasound Probe Tracking for Real-Time Ultrasound/MRI Overlay and Visualization of Brain Shift," Springer, Berlin, Heidelberg, 1999, pp. 920–927.

[40] M. Nakamoto, Y. Sato, and M. Miyamoto, "3D Ultrasound System Using a Magneto-optic Hybrid Tracker for Augmented Reality Visualization in Laparoscopic Liver Surgery," *Med. Image Comput. Comput. Assist. Interv.*, pp. 148–155, 2002.

[41] S. Y. Sun, M. Gilbertson, and B. W. Anthony, "6-DOF probe tracking via skin mapping for freehand 3D ultrasound," in *Proceedings - International Symposium on Biomedical Imaging*, 2013, pp. 780–783.

[42] A. Fenster, D. B. Downey, and H. N. Cardinal, "Three-dimensional ultrasound imaging," *Phys. Med. Biol.*, vol. 46, no. 5, pp. R67–R99, May 2001.

[43] J. a. Noble and D. Boukerroui, "Ultrasound image segmentation: a survey," *IEEE Trans. Med. Imaging*, vol. 25, no. 8, pp. 987–1010, 2006.

[44] M. Mulet-Parada and J. A. Noble, "2D+{T} acoustic boundary detection in echocardiography," *Med. Image Anal.*, vol. 4, no. 1, pp. 21–30, 2000.

[45] T. Binder, M. Süssner, D. Moertl, T. Strohmer, H. Baumgartner, G. Maurer, and G. Porenta, "Artificial neural networks and spatial temporal contour linking for automated endocardial contour detection on echocardiograms: A novel approach to determine left ventricular contractile function," *Ultrasound Med. Biol.*, vol. 25, no. 7, pp. 1069–1076, 1999.

[46] M. Mignotte, J. Meunier, and J.-C. Tardif, "Endocardial Boundary Estimation and Tracking in Echocardiographic Images using Deformable Template and Markov Random Fields," *Pattern Anal. Appl.*, vol. 4, no. 4, pp. 256–271, 2001.

[47] F. U. A. A. Minhas, D. Sabih, and M. Hussain, "Automated classification of liver disorders using ultrasound images," *J. Med. Syst.*, vol. 36, no. 5, pp. 3163–3172, 2012.

[48] Y. Su, Y. Wang, J. Jiao, and Y. Guo, "Automatic detection and classification of breast tumors in ultrasonic images using texture and morphological features.," *Open Med. Inform. J.*, vol. 5, no. Suppl 1, pp. 26–37, 2011.

[49] M. W. Gilbertson, "Electromechanical Systems to Enhance the Usability and Diagnostic Capabilities of Ultrasound Imaging," Massachusetts Institute of Technology, 2014.

[50] A. Y. Huang, "May the Force Be With You: A Medical Ultrasound System with Integrated Force Measurement," Massachusetts Institute of Technology, 2017.

[51] M. W. Gilbertson and B. W. Anthony, “An ergonomic, instrumented ultrasound probe for 6-axis force/torque measurement,” *Conf. Proc. ... Annu. Int. Conf. IEEE Eng. Med. Biol. Soc. IEEE Eng. Med. Biol. Soc. Annu. Conf.*, vol. 2013, pp. 140–143, 2013.

[52] S. Colombo, L. Belloli, M. Zaccanelli, E. Badia, C. Jamoletti, M. Buonocore, and P. Del Poggio, “Normal liver stiffness and its determinants in healthy blood donors.,” *Dig. Liver Dis.*, vol. 43, no. 3, pp. 231–236, 2011.

[53] J. Fung, C. Lee, M. Chan, W. Seto, D. K. Wong, C. Lai, and M. Yuen, “Defining normal liver stiffness range in a normal healthy Chinese population without liver disease.,” *PLoS One*, vol. 8, no. 12, p. e85067, 2013.

[54] A. J. Pigula, J. S. Wu, M. W. Gilbertson, B. T. Darras, S. B. Rutkove, and B. W. Anthony, “Force-controlled ultrasound to measure passive mechanical properties of muscle in Duchenne muscular dystrophy,” in *Proceedings of the Annual International Conference of the IEEE Engineering in Medicine and Biology Society, EMBS*, 2016, vol. 2016–Octob, pp. 2865–2868.

[55] A. J. Pigula, J. S. Wu, K. Kapur, B. T. Darras, S. B. Rutkove, and B. W. Anthony (in press), “Muscle Compression Improves Reliability of Ultrasound Echo Intensity,” *Muscle and Nerve*.

[56] S.-Y. Sun, “Ultrasound Probe Localization by Tracking Skin Features,” Massachusetts Institute of Technology, 2014.

[57] T. Nakayama, S. Kuru, M. Okura, Y. Motoyoshi, and M. Kawai, “Estimation of net muscle volume in patients with muscular dystrophy using muscle CT for prospective muscle volume analysis: an observational study.,” *BMJ Open*, vol. 3, no. 10, p. e003603, 2013.

[58] J. D. Walston, “Sarcopenia in older adults.,” *Curr. Opin. Rheumatol.*, vol. 24, no. 6, pp. 623–7, 2012.

[59] T. Woodard, S. Sigurdsson, J. D. Gotal, A. A. Torjesen, L. A. Inker, T. Aspelund, G. Eiriksdottir, V. Gudnason, T. B. Harris, L. J. Launer, A. S. Levey, and G. F. Mitchell, “Segmental kidney volumes measured by dynamic contrast-enhanced magnetic resonance imaging and their association with CKD in older people,” *Am. J. Kidney Dis.*, vol. 65, no. 1, pp. 41–48, 2014.

[60] J. K. Ghali, “The Prognostic Role of Left Ventricular Hypertrophy in Patients with or without Coronary Artery Disease,” *Ann. Intern. Med.*, vol. 117, no. 10, p. 831, Nov. 1992.

[61] H. M. Behre, J. Bohmeyer, and E. Nieschlag, "Prostate volume in testosterone-treated and untreated hypogonadal men in comparison to age-matched normal controls.," *Clin. Endocrinol. (Oxf).*, vol. 40, no. 3, pp. 341–9, 1994.

[62] M. Zitzmann, M. Depenbusch, J. Gromoll, and E. Nieschlag, "Prostate volume and growth in testosterone-substituted hypogonadal men are dependent on the CAG repeat polymorphism of the androgen receptor gene: A longitudinal pharmacogenetic study," *J. Clin. Endocrinol. Metab.*, vol. 88, no. 5, pp. 2049–2054, 2003.

[63] J. J. Grantham, V. E. Torres, A. B. Chapman, L. M. Guay-Woodford, K. T. Bae, B. F. King, L. H. Wetzel, D. A. Baumgarten, P. J. Kenney, P. C. Harris, S. Klahr, W. M. Bennett, G. N. Hirschman, C. M. Meyers, X. Zhang, F. Zhu, and J. P. Miller, "Volume progression in polycystic kidney disease.," *N. Engl. J. Med.*, vol. 354, no. 20, pp. 2122–30, May 2006.

[64] A. Alam, N. K. Dahl, J. H. Lipschutz, S. Rossetti, P. Smith, D. Sapir, J. Weinstein, P. McFarlane, and D. G. Bichet, "Total kidney volume in autosomal dominant polycystic kidney disease: A biomarker of disease progression and therapeutic efficacy," *Am. J. Kidney Dis.*, vol. 66, no. 4, pp. 564–576, 2015.

[65] A. D. Kistler, D. Poster, F. Krauer, D. Weishaupt, S. Raina, O. Senn, I. Binet, K. Spanaus, R. P. Wüthrich, and A. L. Serra, "Increases in kidney volume in autosomal dominant polycystic kidney disease can be detected within 6 months," *Kidney Int.*, vol. 75, no. 2, pp. 235–241, 2009.

[66] M. A. Makusidi, A. Chijioke, K. T. Braimoh, A. Aderibigbe, T. O. Olanrewaju, and H. M. Liman, "Usefulness of renal length and volume by ultrasound in determining severity of chronic kidney disease," *Saudi J. Kidney Dis. Transplant.*, vol. 25, no. 5, pp. 1117–1121, 2014.

[67] B. Feldt-Rasmussen, L. Hegedus, E. R. Mathiesen, and T. Deckert, "Kidney volume in type 1 (insulin-dependent) diabetic patients with normal or increased urinary albumin excretion: effect of long-term improved metabolic control," *Scand. J. Clin. Lab. Investig.*, vol. 51, no. 1, pp. 31–36, 1991.

[68] A. Fedorov, R. Beichel, J. Kalpathy-Cramer, J. Finet, J. C. Fillion-Robin, S. Pujol, C. Bauer, D. Jennings, F. Fennessy, M. Sonka, J. Buatti, S. Aylward, J. V. Miller, S. Pieper, and R. Kikinis, "3D Slicer as an image computing platform for the Quantitative Imaging Network," *Magn. Reson. Imaging*, vol. 30, no. 9, pp. 1323–1341, 2012.

[69] G. M. Treece, R. W. Prager, A. H. Gee, and L. Berman, "Fast surface and volume estimation from non-parallel cross-sections, for freehand three-dimensional ultrasound," *Med. Image Anal.*, vol. 3, no. 2, pp. 141–173, 1999.

[70] B. Cheong, R. Muthupillai, M. F. Rubin, and S. D. Flamm, "Normal values for renal length and volume as measured by magnetic resonance imaging.," *Clin. J. Am. Soc. Nephrol.*, vol. 2, no. 1, pp. 38–45, Jan. 2007.

[71] S. A. Emamian, M. B. Nielsen, J. F. Pedersen, and L. Ytte, "Kidney dimensions at sonography: Correlation with age, sex, and habitus in 665 adult volunteers," *Am. J. Roentgenol.*, vol. 160, no. 1, pp. 83–86, 1993.

[72] J. Civera, A. J. Davison, and J. M. M. Montiel, "Inverse depth parametrization for monocular SLAM," *IEEE Trans. Robot.*, vol. 24, no. 5, pp. 932–945, 2008.

[73] P. Piniés, T. Lupton, S. Sukkarieh, and J. D. Tardós, "Inertial aiding of inverse depth SLAM using a monocular camera," in *Proceedings - IEEE International Conference on Robotics and Automation*, 2007, pp. 2797–2802.

[74] P. Newman, D. Cole, and K. Ho, "Outdoor SLAM using visual appearance and laser ranging," in *Proceedings - IEEE International Conference on Robotics and Automation*, 2006, vol. 2006, pp. 1180–1187.

[75] D. M. Cole and P. M. Newman, "Using laser range data for 3D SLAM in outdoor environments," *Robot. Autom. 2006. ICRA 2006. Proc. 2006 IEEE Int. Conf.*, pp. 1556–1563, 2006.

[76] M. Li and A. I. Mourikis, "High-precision, consistent EKF-based visual-inertial odometry," *Int. J. Rob. Res.*, vol. 32, no. 6, pp. 690–711, 2013.

[77] M. Li and A. I. Mourikis, "Improving the accuracy of EKF-based visual-inertial odometry," in *Proceedings - IEEE International Conference on Robotics and Automation*, 2012, pp. 828–835.

[78] M. Bloesch, S. Omari, M. Hutter, and R. Siegwart, "Robust visual inertial odometry using a direct EKF-based approach," in *IEEE International Conference on Intelligent Robots and Systems*, 2015, vol. 2015–Decem, pp. 298–304.

[79] P. Tanskanen, T. Naegeli, M. Pollefeys, and O. Hilliges, "Semi-direct EKF-based monocular visual-inertial odometry," in *IEEE International Conference on Intelligent Robots and Systems*, 2015, vol. 2015–Decem, pp. 6073–6078.

[80] G. Gallegos and P. Rives, “Indoor SLAM based on composite sensor mixing laser scans and omnidirectional images,” in *Proceedings - IEEE International Conference on Robotics and Automation*, 2010, pp. 3519–3524.

[81] S. Y. Hwang and J. B. Song, “Monocular vision-based SLAM in indoor environment using corner, lamp, and door features from upward-looking camera,” *IEEE Trans. Ind. Electron.*, vol. 58, no. 10, pp. 4804–4812, 2011.

[82] K. Çelik, S. J. Chung, M. Clausman, and A. K. Somani, “Monocular vision SLAM for indoor aerial vehicles,” in *2009 IEEE/RSJ International Conference on Intelligent Robots and Systems, IROS 2009*, 2009, pp. 1566–1573.

[83] V. Nguyen, A. Harati, A. Martinelli, R. Siegwart, and N. Tomatis, “Orthogonal SLAM: A step toward lightweight indoor autonomous navigation,” in *IEEE International Conference on Intelligent Robots and Systems*, 2006, pp. 5007–5012.

[84] P. Henry, M. Krainin, E. Herbst, X. Ren, and D. Fox, “RGB-D mapping: Using depth cameras for dense 3D modeling of indoor environments,” in *Springer Tracts in Advanced Robotics*, 2014, vol. 79, pp. 477–491.

[85] D. Schleicher, L. M. Bergasa, M. Ocaña, R. Barea, and M. E. López, “Real-time hierarchical outdoor slam based on stereovision and GPS fusion,” *IEEE Trans. Intell. Transp. Syst.*, vol. 10, no. 3, pp. 440–452, 2009.

[86] D. Schleicher, L. M. Bergasa, M. Ocaña, R. Barea, and E. López, “Real-time hierarchical GPS aided visual SLAM on urban environments,” in *Lecture Notes in Computer Science (including subseries Lecture Notes in Artificial Intelligence and Lecture Notes in Bioinformatics)*, 2009, vol. 5717 LNCS, pp. 326–333.

[87] S. Thrun and M. Montemerlo, “The Graph SLAM Algorithm with Applications to Large-Scale Mapping of Urban Structures,” *Int. J. Rob. Res.*, vol. 25, no. 5–6, pp. 403–429, 2006.

[88] J. Langelaan and S. Rock, “Towards Autonomous UAV Flight in Forests,” in *AIAA Guidance, Navigation, and Control Conference and Exhibit*, 2005.

[89] M. Miettinen, M. Ohman, A. Visala, and P. Forsman, “Simultaneous Localization and Mapping for Forest Harvesters,” *Proc. 2007 IEEE Int. Conf. Robot. Autom.*, no. April, pp. 517–522, 2007.

[90] S. Thrun and J. J. Leonard, “Simultaneous Localization and Mapping,” *Springer Handb. Robot.*, vol. 23, no. 7–8, pp. 871–889, 2008.

[91] R. A. Newcombe, D. Fox, and S. M. Seitz, “DynamicFusion: Reconstruction and tracking of non-rigid scenes in real-time,” in *Proceedings of the IEEE Computer Society Conference on Computer Vision and Pattern Recognition*, 2015, vol. 07–12–June, pp. 343–352.

[92] A. Agudo, “Finite Element based Sequential Bayesian Non-Rigid Structure from Motion a a,” *IEEE Conf. Comput. Vis. Pattern Recognit.*, pp. 1418–1425, 2012.

[93] A. Agudo and F. Moreno-Noguer, “Simultaneous pose and non-rigid shape with particle dynamics,” in *Proceedings of the IEEE Computer Society Conference on Computer Vision and Pattern Recognition*, 2015, vol. 07–12–June, pp. 2179–2187.

[94] A. Agudo, F. Moreno-Noguer, B. Calvo, and J. M. M. Montiel, “Sequential Non-Rigid Structure from Motion Using Physical Priors,” *IEEE Trans. Pattern Anal. Mach. Intell.*, vol. 38, no. 5, pp. 979–994, 2016.

[95] L. A. Chai, “Design of Mechanical Arterial Simulator,” Massachusetts Institute of Technology, 2012.

[96] G. Bradski, “The OpenCV Library,” *Dr Dobbs J. Softw. Tools*, vol. 25, pp. 120–125, 2000.

APPENDICES

Appendix A.1 Characterization GE Pose Tracking System

This description uses three different body coordinate systems: $x_{i,a}$ for the electromagnetic antenna, $x_{i,p}$ for the US probe, and $x_{i,g}$ for the motion guidance platform. Motions were controlled manually with the help of the guidance platform.

Isolated translations:

The motion patterns for these sequences were defined with respect to the coordinate system on the motion guidance platform as follows: starting at the origin, move 6 in in $x_{1,g}$-direction; return to origin; move -6 in in $x_{2,g}$-direction; return to origin; move 6 in in $x_{2,g}$-direction; return to origin; move 6 in in $x_{3,g}$-direction; return to origin. Translations only, no rotations. This pattern was repeated for different relative positions between the guidance platform and the antenna; and the guidance platform and the probe. The relative positions (prior to the start of the recording) explored are listed below. All experiments except case 1.4 were done at least twice each.

Case 1: align $x_{i,g}$to be parallel to $x_{i,a}$

Case 1.1: align $x_{1,p}$ to be parallel to $x_{1,g}$

Case 1.2: align $x_{2,p}$ to be parallel to $x_{1,g}$

Case 1.3: align $x_{3,p}$ to be parallel to $x_{1,g}$

Case 1.4: align $x_{3,p}$ to be parallel to $x_{1,g}$; rotate probe by 180 ° around $x_{3,a}$

Case 2: align $x_{1,g}$ to be parallel to $x_{i,a}$, then rotate guidance platform around $x_{3,a}$ by 45 °

Case 2.1: align $x_{1,p}$ to be parallel to $x_{1,g}$

Case 2.2: align $x_{2,p}$ to be parallel to $x_{1,g}$

Case 2.3: align $x_{3,p}$ to be parallel to $x_{1,g}$

Case 3: like Case 1.1, but guidance platform rotated around $x_{3,a}$

Case 4: like Case 1.1, but guidance platform rotated around $x_{1,a}$, $x_{2,a}$, $x_{3,a}$

Isolated rotations:

Upon starting the recording, the probe was then rotated (no translation) around a select probe axis as follows: rotate (in positive direction) by 90 °; rotate back to starting pose; rotate by 180 °; rotate back to starting pose. All experiments were done twice each.

Case 5: prior recording, placed probe such that axes $x_{i,p}$ were parallel to axes $x_{i,a}$

- **Case 3.1:** rotate around $x_{1,p}$
- **Case 3.1:** rotate around $x_{2,p}$
- **Case 3.1:** rotate around $x_{3,p}$

Case 6: prior recording, placed probe such that axes $x_{i,p}$ were parallel to axes $x_{i,a}$, then rotated probe by 45 ° around $x_{3,a}$

- **Case 4.1:** rotate around $x_{1,p}$
- **Case 4.1:** rotate around $x_{2,p}$
- **Case 4.1:** rotate around $x_{3,p}$

Combined translations and rotations:

Case 7: align $x_{i,g}$to be parallel to $x_{i,a}$; align $x_{i,p}$to be parallel to $x_{i,a}$; rotate probe around $x_{3,a}$ by 90 ° such that $x_{2,p}$ is parallel to $x_{1,g}$; start recording; rotate probe by -90 ° around $x_{3,a}$ such that $x_{1,p}$ is parallel to $x_{1,g}$; follow translation pattern as described for Case 1

Appendix A.2 Phantom Fabrication

Precursor materials:

- Kraton ThermoRubber Copolymer (5 parts by weight)
- Food grade mineral oil (100 parts by weight)

Process steps:

1. Preheat mold to 130 °C
2. In a beaker, dissolve Kraton Copolymer in oil and mix thoroughly to achieve uniform suspension
3. Place beaker in oil bath on hot plate. Heat oil bath to 130 °C
4. Maintain elevated temperature and wait for copolymer to dissolve completely
5. Pour mixture into preheated mold
6. Bake in oven at 130 °C until air bubbles have risen out of mixture
7. Remove from oven
8. Let cool down at room temperature
9. Remove phantom from mold, once both have reached room temperature